MULTISCALE HYBRID SUPERPIXEL METHOD FOR PRE-PROCESSING AND SEGMENTATION OF BREAST TUMORS IN ULTRASOUND IMAGES

BY

Mr. ADEMOLA ENITAN ILESANMI

A DISSERTATION SUBMITTED IN PARTIAL FULFILLMENT OF THE REQUIREMENTS FOR THE DEGREE OF DOCTOR OF PHILOSOPHY (ENGINEERING AND TECHNOLOGY)

SIRINDHORN INTERNATIONAL INSTITUTE OF TECHNOLOGY
THAMMASAT UNIVERSITY
ACADEMIC YEAR 2020

MULTISCALE HYBRID SUPERPIXEL METHOD FOR PRE-PROCESSING AND SEGMENTATION OF BREAST TUMORS IN ULTRASOUND IMAGES

BY

Mr. ADEMOLA ENITAN ILESANMI

A DISSERTATION SUBMITTED IN PARTIAL FULFILLMENT OF THE REQUIREMENTS FOR THE DEGREE OF DOCTOR OF PHILOSOPHY (ENGINEERING AND TECHNOLOGY)
SIRINDHORN INTERNATIONAL INSTITUTE OF TECHNOLOGY
THAMMASAT UNIVERSITY
ACADEMIC YEAR 2020

THAMMASAT UNIVERSITY
SIRINDHORN INTERNATIONAL INSTITUTE OF TECHNOLOGY

DISSERTATION

BY

MR. ADEMOLA ENITAN ILLESANMI

ENTITLED

MULTISCALE HYBRID SUPERPIXEL METHOD FOR PRE-PROCESSING AND SEGMENTATION OF BREAST TUMORS IN ULTRASOUND IMAGES

was approved as partial fulfillment of the requirements for
the degree of Doctor of Philosophy (Engineering and Technology)

on June 2, 2021

Chairperson ______________________
(Associate Professor Annupan Rodtook, Ph.D.)

Member and Advisor ______________________
(Professor Stanislav S. Makhanov, Ph.D.)

Member ______________________
(Associate Professor Waree Kongprawechnon, Ph.D.)

Member ______________________
(Associate Professor Toshiaki Kondo, Ph.D.)

Member ______________________
(Associate Professor Pakinee Aimmanee, Ph.D.)

Director ______________________
(Professor Pruettha Nanakorn, D.Eng.)

Thesis Title	MULTISCALE HYBRID SUPERPIXEL METHOD FOR PRE-PROCESSING AND SEGMENTATION OF BREAST TUMORS IN ULTRASOUND IMAGES
Author	Ademola Enitan Ilesanmi
Degree	Doctor of Philosophy (Engineering and Technology)
Faculty/University	Sirindhorn International Institute of Technology/Thammasat University
Thesis Advisor	Professor Stanislav S. Makhanov, Ph.D.
Academic Years	2020

ABSTRACT

Background The ultrasound test for cancer screening is low-cost and non-invasive. A major drawback is that multiplicative speckle noise can jeopardize the efficiency of the test. This research proposes a new algorithm to reduce noise and segment breast ultrasound.

Methods The method is in two stages. Stage one is based on a combination of the multiscale approach, the Wiener filter, and a new combination of wavelet-transform denoising and the anisotropic Perona-Malik-type filter. In the second stage, pre-processed image is transformed into multiscale images, and then, a boundary efficient superpixel decomposition of the multiscale images is created. Finally, the tumor region is generated by the boundary graph cut segmentation method.

Results The algorithm has been tested on 50 synthetic images degraded by speckle noise with varying intensity and 250 breast ultrasound (BUS) images from two datasets. The results are compared with selected state-of-the-art filters. The proposed approach shows better performance in terms of standard evaluation measures. The results are compared with ground truth by the DICE coefficient, the Jaccard coefficient, and the Hausdorff distance. The proposed filter also achieves high accuracy in terms of these segmentation measures.

Conclusions The proposed two-stage algorithm achieves better accuracy, compared to selected state-of-the-art methods applied to BUS images.

Keywords: Speckle noise reduction; Multiscale algorithm; Breast ultrasound images, Superpixel Decomposition**;** Graph Cut.

ACKNOWLEDGEMENT

Foremost, I want to express my sincere gratitude to God Almighty for giving me the strength to start and complete this project.

I wish to acknowledge **Prof. Dr. Stanislav S. Makhanov,** my advisor whose advice and passionate supervision of the project helped to complete it. Thank you, Sir!. I also wish to express my profound gratitude to all my thesis committee members and all lecturers in the department of ICT.

Furthermore, I remain grateful to **Mrs. Alice Kehinde Ilesanmi,** my mother, and my late father **Barrister Kunle Ilesanmi** for the love, advice, and encouragement during my study. I am also grateful to my wife **Taiwo Ilesanmi**, my daughter **Shindara Ilesanmi** and my siblings; **Segun Ilesanmi**, **Goke Ilesanmi**, and **Wale Ilesanmi**, who stood by me always in times of trial, thank you all.

Ademola Enitan Ilesanmi

TABLE OF CONTENTS

LIST OF TABLES

LIST OF FIGURES

CHAPTER 1
INTRODUCTION

1.1 Background

Medical imaging is a process to obtain the internal structure and interior of the human organs. Recently, medical imaging has developed very quickly due to image processing techniques. Image recognition, image enhancement, and image analysis have helped to improve medical diagnosis. For example, these techniques have helped in detecting early-stage cancers. In 2018, the World Health Organization estimated that cancer was the second leading cause of death globally. Cancer amounts to 9.6 million deaths, equating to approximately one out of six deaths globally. In the same year, breast cancer death was estimated at 627,000. Breast cancer in developing countries contributes to the majority of these figures. To prevent and survive death from breast cancer, clinicians advocate early detection, diagnosis, and treatment (Qi et al., 2019).

Ultrasound is an effective tool to detect cancers. The ultrasound device generates sound waves and records echoes to produce a pictorial representation of the internal organs. Ultrasound is to determine the gender of a baby in the womb, to diagnose the abnormalities in the breast, pelvic, kidney, transrectal, liver, gallbladder, carotid, etc. The advantages of ultrasound include noninvasive, radiation-free use. Huang et al. (2020) opine that the numerous advantages of ultrasound make it one of the preferred imaging techniques in clinical diagnosis.

Undoubtedly, the most effective procedure of image segmentation in medical practice is the manual process. When performing manual segmentation the experienced radiologists rely on experience and medical knowledge. Unfortunately, manual segmentation is time-consuming and laborious. This gave rise to the Computer-aided diagnosis (CAD) system.

A CAD is a computer system built to speedily assist clinicians to interpret medical images. CAD uses computer vision, medical image processing, and artificial intelligence techniques for diagnosis. However, CADs are not to replace doctors or clinicians but to assist and support them as a second interpreter (Huang et al., 2018).

The general procedure to find the Region of Interest (ROI) using CAD for BUS images is depicted in Fig.1.

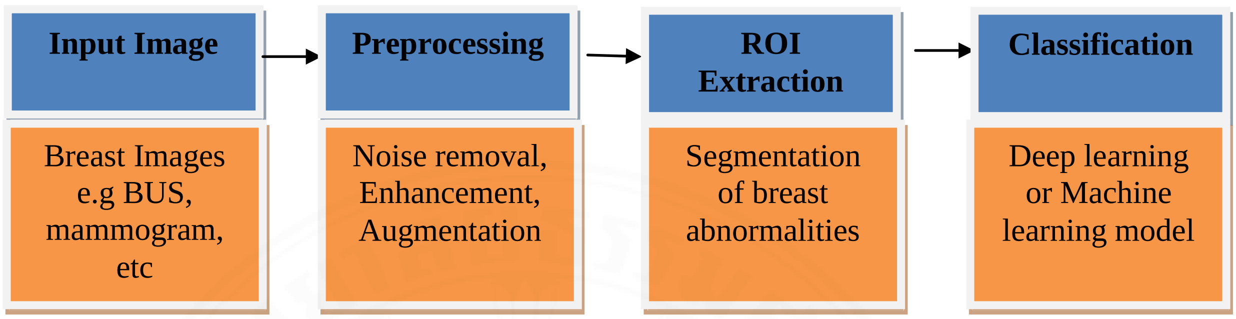

Fig.1. Block diagram of CAD for breast cancer

Despite the advent of CADs, the segmentation task is still challenging. This is due to speckle noise, acoustic shadow effects, changes of the tumor shape and size, appearance, and texture. The major obstruction to effective segmentation of BUS image is the speckle noise (generating granular patterns). This type of noise originates from echoes in the ultrasonography making the ultrasound difficult for further processing (Wang et al., 2018). Examples of BUS images corrupted by the noise are shown in Fig. 2.

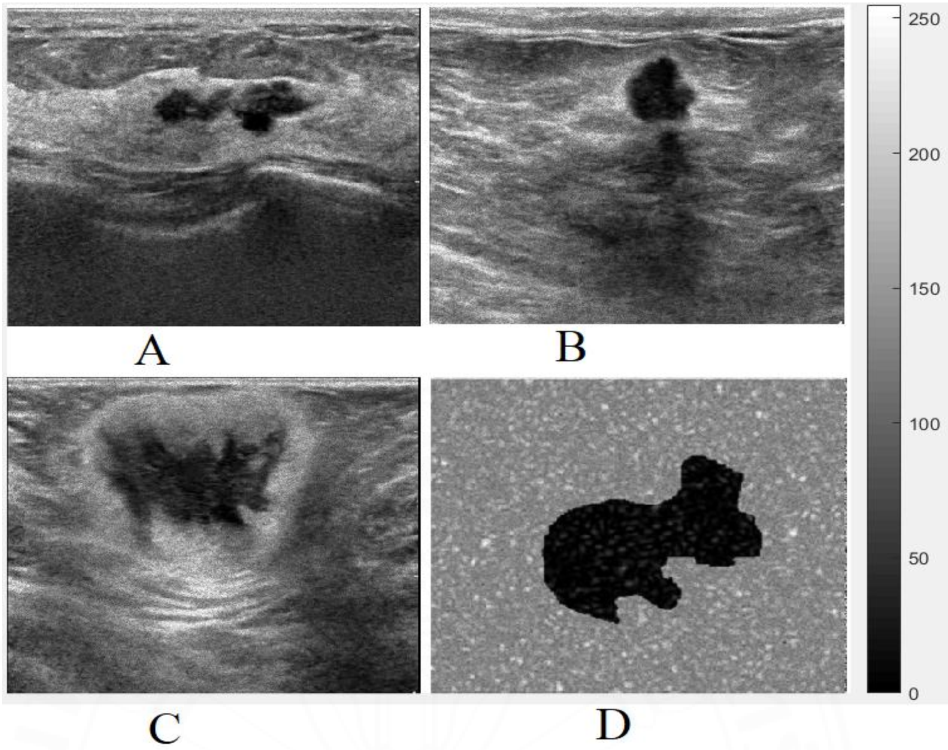

Fig. 2. Speckle noise in BUS images (A) – (C) speckle noise in the BUS images (D) speckle noise in a synthetic image

To reduce speckle noise two important approaches have been used: the compound approach (Mateo et al., 2009) and the post-processing approach (Adam et al., 2006). The compound approach performs speckle reduction using several images of the same region and thereafter combining them into a single image. Meanwhile, the post-processing approach offers a variety of digital filters.

Filters are systematic computer vision techniques designed to improve the appearance of images. They operate by removing unwanted changes from the image to give it a better output (De-Fontes et al., 2011). The examples are bilateral filter (Ghosh &Chaudhary, 2016), anisotropic filter (Dore, Moghaddam, & Cheriet, 2011), median filter (Arias-Castro & Donoho, 2009), wavelet-based filters (Vidya et al., 2016), Lee, Kaun and Wiener filters (Anita et al., 2011). However, there are specific filters designed for different types of medical images. Some filters are not appropriate for the ultrasound images (Tania and Rowaida, 2016). Therefore, it is important to design filters specifically for ultrasound images.

1.2 Problem Statement

Develop and verify preprocessing and segmentation algorithms for ultrasound images of breast abnormalities based on the superpixel approach.

1.3 Purpose of the Study

This research is expected to create an algorithm to pre-process and segment BUS images. We prove the advantages of the proposed method i.e. stability, robustness, efficient edge preservation, artifact removal, and accurate tumor delineation.

1.4 Significance of the Study

This model is useful in clinical medicine such as ultrasound surgery navigation and diagnosis. The findings of this study are helpful to

Computer Vision Analyst The method improves accuracy and provides unbiased results which the analyst can easily understand and improve.

Clinicians Results of this study are promising and may help clinicians to improve the decision-making process.

Future Researcher The study helps future researchers to uncover the critical areas in medical image processing.

CHAPTER 2
LITERATURE REVIEW

2.1 Review of Speckle Reduction Filters

Speckle reduction filters are becoming sophisticated and advanced. For example, image patch filters have gained prominence for noise removal. The research by Baseline et al., (2015) is an example of filtering by patches. The major advantage is effective noise removal and edge preservation. Hybrid algorithms remove the noise by combining several filters. Nageswari and Prabha (2013) use a hybrid filter that combines the MF, WF, and the Frost filter (Talha, Sulong, & Jaffar., 2016). A comprehensive review of speckle noise reduction algorithms is available in Gai, Zhang, and Yang (2018). They reduce the speckles by combining the Monogenic Wavelet Transform and the Bayesian framework. The wavelet coefficients are modeled by the Laplace distribution. The Bayesian framework is based on the mean square error and the expectation maximization. Avanaki et al., (2013) combine random pixel selection and the MF. Adabi et al., (2018) apply the Learnable De-specking Framework to rank and use a combination of the filtering algorithms. The algorithm uses quality assessment methods (example of quality assessment methods: structural similarity Index, Peak signal-to-noise ratio, etc.) to measures the quality of images. The SVM classifier is used to select the best filter. Finally, the research by Eybposhet al., (2018) used the Cluster-based Speckle Reduction Framework. The algorithm consists of clustering and de-specking. The K-means clusters the pixels, the MF removes small clusters. Finally, a combination of the Lee filter and adaptive WF removes the speckles.

Bajaj, Singh, and Ansari (2019) use the autoencoder method which emulates the learning process of noise by mimicking the noise patterns associated with the image. The architecture consists of 10 convolutional and 2 deconvolution layers. A single convolution precedes the input and output layers. The autoencoder removes the noise by learning from the past noise patterns.

Hong, Hwang, and Kim, (2019) employ an ensemble strategy for exploiting multiple deep neural networks in image denoising. First, the image denoising task is divided into subtasks based on the complexity of the image patches and conquers for each subtask. The subtasks are combined based on the likelihood of each network. Next, the patches are concatenated for the input of the patch classifier, and the output is used to combine the denoised patches by a weighted sum.

Fang and Zeng, (2020) combine the convolutional neural network (CNN) with a variation regularized model. Prior knowledge is retrieved from the noisy image. Subsequently, the edge regularization and the total variation approach are combined. Finally, the authors use the split Bregman method to clean the image. In a nutshell, a CNN is used to extract the designed edge features from noisy images; while the total variation regularization method denoised the edges.

Lyu, Zhang, and Han, (2020) use the U-Net (Ronneberger, Fischer, & Brox, 2015) and a nonsubsampled contourlet transform (NSCT) to remove the noise. Unlike most deep learning networks, the algorithm does not have max pooling and upsampling. The NSCT and inverse NSCT are used instead of them. The model applies convolution, batch normalization, rectified linear unit (ReLu), NSCT, and the inverse NSCT. Gai and Bao, (2019) combine the joint loss function (MSE and perceptual loss (Wu et al., 2018)) with a deep convolutional neural network. The end-to-end adaptive residual CNN is constructed. The features are extracted by the adaptive convolution and a leaky ReLu. The initial denoised image is obtained using the mean square error (MSE). Finally, a pre-trained SegNet and a perception loss function produce the denoised image. The method has one residual and convolution layer, 2 ReLu layers, and 3 leaky ReLu layers. The number of layers has been obtained experimentally. Xie, Li, and Jia, (2018) used a CNN, residual learning, and batch normalization. Clean and noisy images are used as the input in the learning stage while the denoised stage and mapping strategy is adopted to reconstruct the image. The spectral difference, key selection, and above denoising are the key components of this method.

Lee, et al., (2020) remove the noise at different scales by a modification of the U-Net method. First, a multiscale pyramid is created and passed to the U-Net. The residual method is applied to denoise the pyramid and produce a clean image. A performance improvement is achieved based on the coarse-to-fine segmentation. Wu et al., (2020) propose an end-to-end deep neural network. The model uses the multiple tunable noise level as input and outputs a clean image. The model is trained by simultaneous bucket signals and ground truth pairs, and then the object is retrieved from experimental one-dimensional bucket signals. Tian, Xu, and Zuo, (2020) propose a batch-renormalization denoising network. The model combines two networks. Batch renormalization is the key component used to accelerate convergence of the networks. The model uses a dilated convolution to enlarge the reception field and to treat vanishing or exploding gradients. The network consists of 18 layers (two convolution layers, four dilation layers, and ten batch renormalization layers).

Zhang, et al., (2019) proposed a variant of the stabilizing transform network. The model uses the stabilization transform (Azzari &Foi, 2016). It consists of three sub-networks with learnable and frozen patterns. The first and third sub-networks use the Anscombe transformation technique (Anscombe, 1948), while the second sub-network approximates the Gaussian denoising patterns. The second sub-network consists of 7 layers, while the first and third have 3 layers each.

Ahmed, (2018) combines the adaptive thresholding, the nonlinear diffusion technique, and the discrete shearlet transform. A multiscale decomposition generates eight bands. Adaptive thresholding is used to obtain discrete shearlet transform coefficients. Finally, the image is reconstructed by the inverse transform.

2.2 Review of BUS Segmentation

A large body of research exists for the segmentation of BUS images. In this study, we have classified these methods into four categories: graph-based methods (Pons et al., 2016), deformable models (DM) (Gao et al., 2012), semantic segmentation methods, and classical methods (Fig. 3).

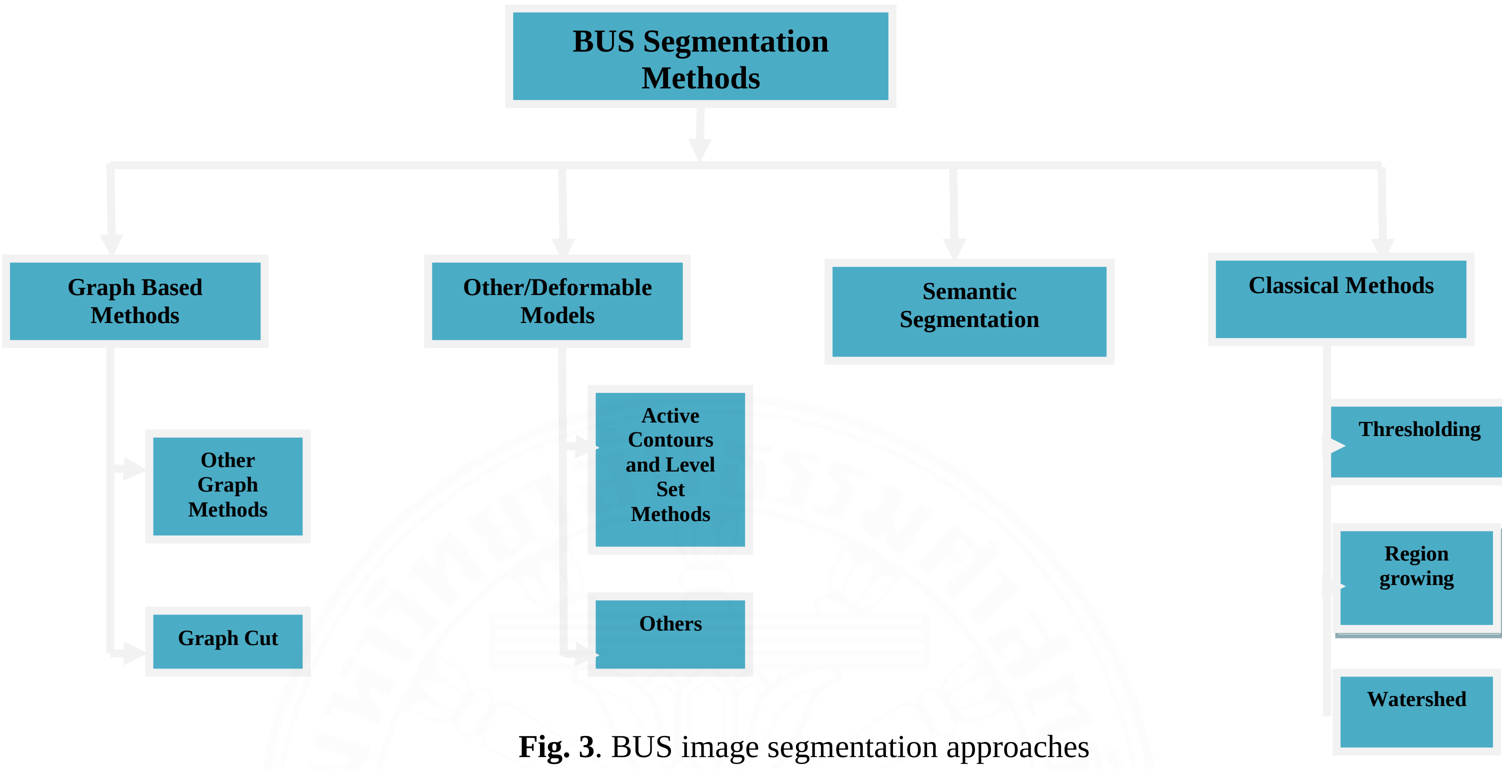

Fig. 3. BUS image segmentation approaches

2.2.1 Graph-based Methods

Advantages of graph-based methods include simplicity, flexibility, and the possibility to include optimization constraints. The Markov random field, the graph cut, and the normalized graph cut are examples of graph-based methods. Lee et al. (2010) propose a segmentation method that uses three phases. The Nonlinear Coherent Diffusion filter is used to reduce noise. Next, a combination of the isotropic diffusion, anisotropic diffusion, and the mean curvature motion methods is applied. The second phase employs a segmentation graph. A calculation of the transverse and pixel edges is generated. Then, the image is mapped to the graph with a modified pair-wise region comparison predicate (Felzenszwalb & Huttenlocher, 2004). Next, the region whose intensities and locations are close to each other are merged with the minimum spanning trees algorithm (Felzenszwalb & Huttenlocher, 2004)

Zhang et al., (2014) propose a graph-based method using particle swarm optimization. The BUS image is cropped and the objective function is formulated using pair-wise parameter combinations based on simulated annealing (Scott, Gelatt,

& Mario, 1983). The particle swarm optimization based on the proposed objective function segments the image.

Daoud et al., (2019) use anisotropic diffusion for speckle reduction. Next, superpixels are generated on the edge map. A combination of the posterior likelihood and graph cut algorithms performs the initial segmentation. The posterior likelihood algorithm extracts gray level co-occurrence matrix features from superpixels, and the features are classified by the SVM. The graph cut algorithm segments the tumor. Next, the edge map is generated again and the procedure is repeated. Finally, the active contour outlines the tumor using the results of the graph cut as the initial contour.

Huang et al., (2012) reduce speckle noise by the nonlinear anisotropic diffusion. Their graph method employing 8-connected pixels is combined with the pair-wise region comparison method. A minimum spanning tree is obtained with the Kruskal method (Kruskal, 1956). Huang et al., (2014) combine the graph method and the particle swarm optimization. Several iterations of the robust graph-based algorithm and particle swarm optimization are performed to improve the accuracy. Zhoul et al., (2014) reduce the speckle noise by the Gaussian filter. Subsequently, image enhancement is performed with the histogram equalization and the mean shift method. To outline the foreground and tumor boundaries, seeds are placed on the image. Finally, the graph cut method segments the image. Overall, graph-based segmentation methods are accurate and effective. Unfortunately, they are gradually becoming less popular in image processing tasks due to the emergence of deep learning methods.

2.2.2 Other/Deformable models

Deformable models (DM) use a curve or a surface moving towards the object boundary under the influence of an external force.

The two types of DM are parametric and geometric DM. The parametric DM represents curves and surfaces explicitly during the deformation. Adaptation of the model topology, however, such as splitting or merging presents difficulties. Geometric DM can handle topological changes automatically based on the theory of curve evolution and the level set theory. Despite these differences, the basic ideas of both methods are very similar

Examples of DM are snakes, active contour, gradient vector fields (Daoud et al., 2012), edge-based DM, and region-based DM. Xian et al., (2015), propose a method to preprocess and find the ROI of BUS images. A low-pass Gaussian filter is used to smooth the BUS images. Next, a linear normalization algorithm combined with the Z- shape function is used for image enhancement. To further enhance the images, a morphological reconstruction is adopted. Then initial reference point is used to search the seed, while a multipath search algorithm is used to obtain the seed inside the tumor. Subsequently, a cost function applies to the candidate ROI subject to frequency constraints. The optimized edge detector algorithm segments the image.

Ramadan et al., (2020), use the salient guided method for segmenting BUS images. The contrast limited adaptive histogram equalization (CLAHE) enhances the images. The speckles are reduced by the optimized Bayesian non-local means filter. The object boundary is set with saliency detection and tumor seeds. Next, the lazy snapping algorithm (Li et al., 2004) generates the initial segmentation. Finally, active contour detects the tumor. Karunanayake et al., (2020) proposed a method that uses the Walking Particle (WP) method for edge-based segmentation. The WP incorporates a continuous diffusion model and the multi-agent system to perform edge-based segmentation on BUS images. The WP is inspired by the epidemiology theory. Keatmanee et al., (2019) fuse the ultrasound, Doppler, and Elastography images to improve the efficiency of the DM. Rodtook et al., (2018), use the combination of the exploding seeds and active contour/level set. Zhao et al., (2020) improve the Distance Regularized Level Set Evolution (DRLSE) algorithm for BUS image segmentation. The noise is reduced by analyzing the multiscale gradient field. A modified improved balloon force improves conventional DRLSE. Rodrigues et al., (2015) extract the features using the non-linear diffusion, bandpass filter, and scale-invariant mean curvature. The initial segmentation is achieved by the SVM and discriminate analysis. The second stage uses AdaBoost and the active contours. Wang et al., (2014), use multiscale geodesic active contours. To avoid boundary leakage, a boundary shape similarity measure has been used by the pyramid decomposition. A geodesic active contour detects the tumor.

Guo et al., (2015), use the neutrosophic similarity (NS) scores and level set algorithms. A three membership subset (T, I, and F) is used to transform the BUS image to the NS domain. After the transformation process, a neutrosophic similarity score of the images in the NS domain is calculated. The level set algorithm segments boundaries.

Panigrahi et al. (2019) use the Gaussian kernel and vector fields and a clustering algorithm that combines the multiscale images with the Gaussian kernel induced by the fuzzy C-means (FCM).

Huang et al. (2014) combine object detection techniques and active contours. The speckle noise is removed by the total variation filter. Graph segmentation is used to divide the images into sub-regions. Object recognition applies to perform the initial segmentation. An active contour identifies the tumor.

Lang et al. (2016) use a four-step multiscale level set segmentation algorithm. The ROI is manually delineated by a radiologist. A multiscale response map (based on texture measure) is created. Subsequently, the level set algorithm is used. Morphological opening and the convex hull algorithm perform post-processing.

Lai et al. (2013) propose a combination of the level set and the morphological operator. The speckle noise is removed by the sigmoid and gradient filters. A morphological operator is used at the final stage. Moon et al. (2013) offer a similar technique. Kriti et al. (2019) use the Chan Vese active DM to segment BUS images. Selvan and Devi, (2015) use the seed point technique. The Speckle Reduction Anisotropic Diffusion (SRAD) (Yongjian & Scott, 2002) removes the speckle noise. The seed points are selected and a gray-value threshold is obtained. The level set surfaces are run with selected seeds.

Liu et al. (2018) use the fuzzy cellular automata framework. Rodtook and Makhanov (2013) propose a variant of the gradient vector flow algorithm. The diffusion term is a combination of the intensity of the edge map and the orientation field. The features are integrated into the generalized gradient vector flow equations (Xu & Prince, 1998).

Overall, the level set and active contour are prominent segmentation algorithms for segmenting BUS images. They maintain one of the leading positions in BUS image segmentation.

2.2.3 Semantic segmentation method

Segmentation problems are solved by grouping pixels characterized by the same structure and color. The learning methods are categorized as: supervised and unsupervised. The K-means and the FCM are examples of the unsupervised methods, while the SVM, the artificial neural network (ANN), Naïve Bayesian classifier, and CNN are examples of supervised methods. Vakanski, Xian, and Freer, (2020) used a combination of the attention gate and the UNet. The upsampled layer is used by the decoding blocks, while the attention gate is used in each block of the encoder.

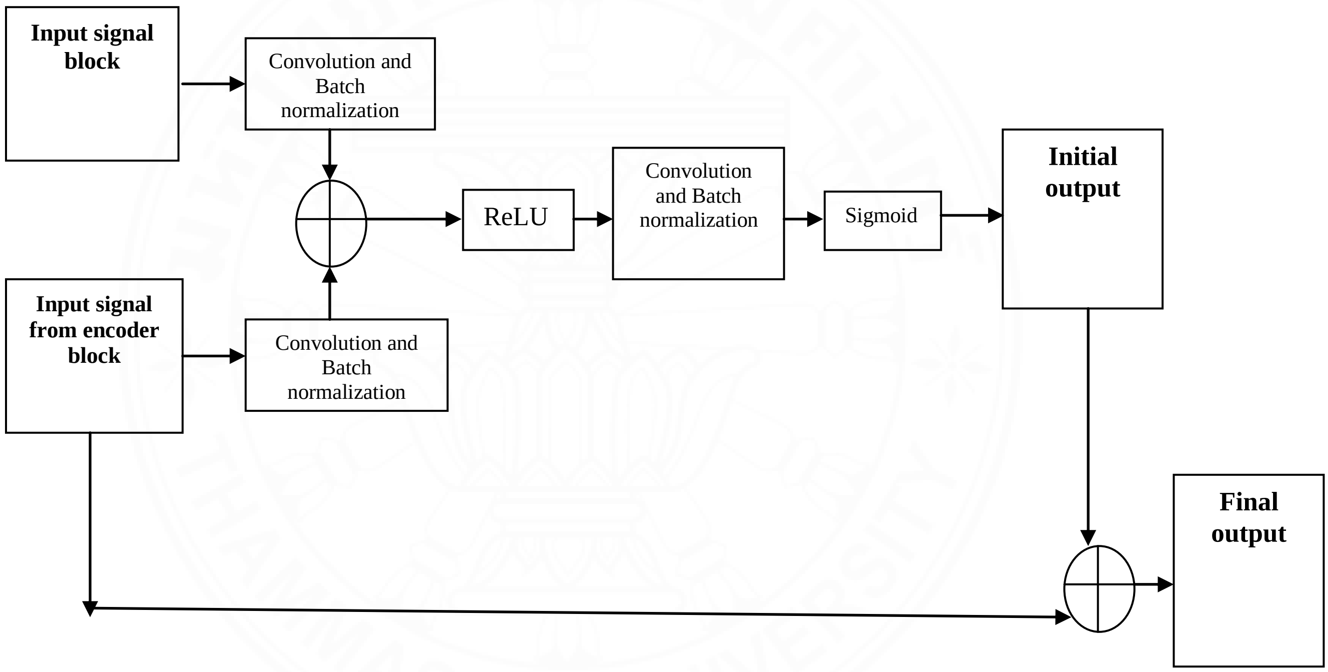

Fig. 4. Diagram of Attention gate architecture

Byraet al., (2020) propose the SK-UNet with the encoding and decoding block. The SK block uses the batch normalization, ReLU, FC layer, and global average pooling. The network consists of 12 convolutions. The SK block mimics the attention gate however its layers have been arranged differently.

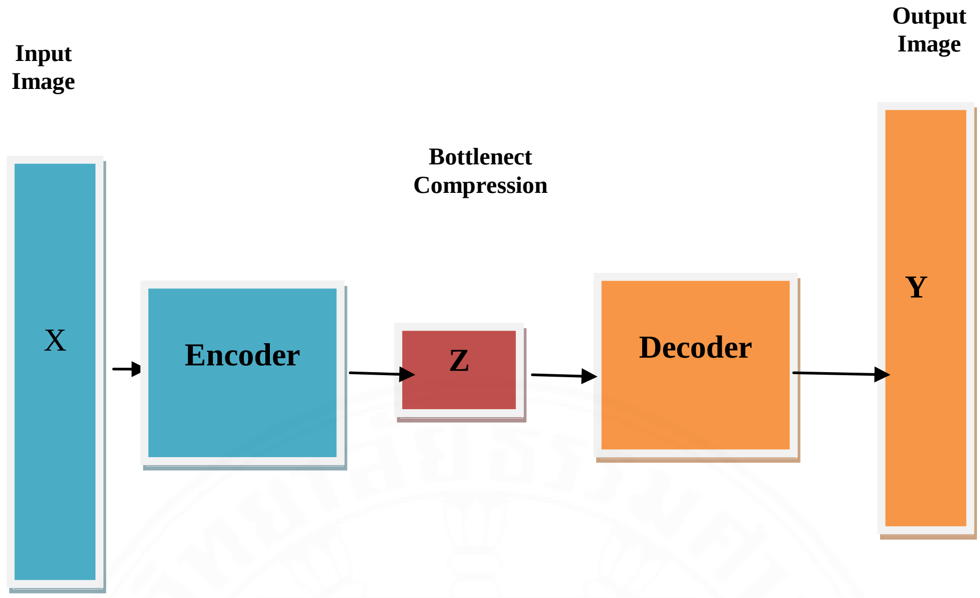

Fig. 5. Block diagram of UNET architecture

Osman and Yap (2020) use a combination of deep learning and Frost filters. The improved mean shift method segments the image and is combined with the binary thresholding. The deep learning phase includes the UNet architecture and the fully connected network (FCN-AlexNet).

Singh et al. (2020) propose a context aware deep adversary learning. The spatial and multi-scale components are captured by the Atrous convolution (Chen et al., 2017). The relevant features are extracted by channel attention and channel weighting (Hu et al., 2018). The network consists of four convolution blocks with an upsample layer.

Han et al. (2020) propose the dual-attentive Generative adversarial network algorithm. The method includes a segmentation network and evaluation network to estimate the segmentation quality of the input. An adversary learning is arranged between the two to maximize the segmentation accuracy.

Kumar et al. (2018) use the CNN and an improved UNet algorithm to segment the ROI. This method is a new modification of the UNet relying on downsampling of the original image. A weighting pixel procedure by the majority voting produces the final output. Hiramatsu et al., (2017) propose an AlexNet. The MF is used for pre-processing. Then hysteresis smoothing is performed and the anisotropic diffusion filters the image. A region growing method is applied to the filtered image. Finally, the AlexNet having 5 convolutional layers and 3 max-pooling layers is applied.

Jiang et al. (2012) propose a combination of the Adaboost classifier (24 Haar features), the k-means clustering algorithm, and the SVM. A random walk algorithm produces a tumor boundary. Further details can be found in the reviews (Xian et al., 2018 and Meiburger et al., 2018).

2.2.4 Traditional/classical methods

Thresholding method, region growing, and watershed methods are popular classical methods in BUS image segmentation. A thresholding algorithm is frequently used to segment BUS images. It is one of the simplest methods in image processing and is based on a threshold value technique that transforms gray-scale images into binary images. Thresholding methods consider gray-level statistics and do not take spatial location information in images. A sample segmentation results with the thresholding method is depicted in Fig. 6.

Maolood et al. (2018) propose the thresholding based on fuzzy entropy formulation combined with the level set approach. Gomez-Flores and Aruiz-Ortega (2016) segment breast tumors by iterative thresholding. The image is preprocessed using the average radial derivatives (Drukker et al. 2002) and then the CLAHE algorithm (Pizer et al. 1987). Interference based speckle filter and the negative of the filter are used for pre-processing.

Yap, Edirisinghe, and Bez (2008) use a hybrid filter, multifractal processing, and thresholding segmentation to detect the ROI. First, histogram equalization (Kim, 1997) is used to achieve homogeneity on the BUS image. The diffusion filter (Perona & Malik, 1990) and the linear filter (Gaussian blur) are used to reduce speckles, smooth edges, and eliminate over-segmentation. Next, multifractal processing (Mandelbrot, 1982) is used to analyze the image to finer scales. Finally, the image is thresholded.

Overall, the thresholding method is effective in BUS image segmentation for simple images. The effective segmentation by the thresholding method includes (1) selecting an empirical value for the dataset, (2) selecting an efficient thresholding parameter, (3) generating the threshold automatically using the statistical-decision theory.

Recently, thresholding methods are now used as a step in segmentation and are rarely used as a standalone method. Many researchers have combined thresholding algorithms with other methods to produce better segmentation results. For example, Mustaqueen, Javed, and Fatima (2012) combine thresholding with watershed, Filipczuk, Kowal, and Obuchowicz (2011) combine thresholding with fuzzy clustering, Altarawneh et al. (2014) combine thresholding with active contour, while Dirami et al. (2013) combine thresholding with level set method. Jain and Singh (2020) employ the threshold rule and wavelet transform for speckle noise reduction. A soft and hard thresholding rule is proposed. The hard thresholding rule produces over-smoothed images and discontinuous thresholds “T” and “-T” using the Gibbs phenomenon (Gibbs, 1925). Meanwhile, the hard thresholding rule uses a constant bias that exists between the original and modified wavelet coefficient. Subsequently, a discrete wavelet is performed over a noisy image, then the noise variance and threshold values are calculated. Finally, the proposed threshold rule is applied with the inverse wavelet transform to reduce speckle.

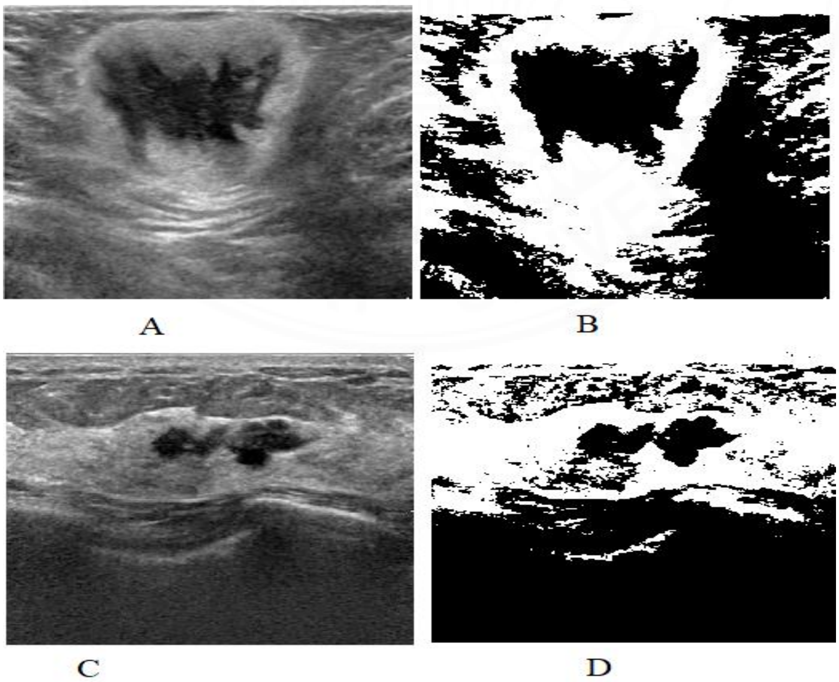

Fig. 6. BUS images with thresholding algorithm. (A) and (C) Original image, (B) and (D) Thresholding of (A) and (B)

The region growing method grows seeds to a bigger region by extracting regions from a set of pixels with established criteria. Kwak, Kim, and Kim (2005) proposed a region growing cost minimization method for segmenting BUS images with ambiguous boundaries intensity variation. The image is divided into initial seed regions. Then, seeds are expanded until it reaches the boundary of the region to maximize the homogeneity of the region and smoothness of the contour.

Shan, Cheng, and Wang (2008) use a new automatic seed point selection and region growing method. First, SRAD is used for speckle reduction. Then, an iterative threshold selection method (Ridler & Calvard, 1978) separates the foreground from the background. Next, the boundary-connected regions (connected components) are deleted and regions are ranked. Finally, segmentation is determined by the region growing algorithm. Madabhushi and Metaxas (2002) used hybrid segmentation for tumor detection in BUS images. A second-order Butterworth filter (Tang, Zhuang & Wu, 2000) reduces the speckles. The histogram equalization enhances the boundary between lesions and surrounding regions. Finally, the combination of different segmentation methods (intensity and texture classification (Stan et al. 1995), seed point determination, region growing, boundary seed location, and deformable model (Chen & Metaxas, 1998)) detect the tumor.

Massich et al. (2010) use a region growing algorithm for initial segmentation, while the Gaussian constraining segmentation (Horsch et al. 2001) performs the final segmentation. An empirical rule (Stavros, Rapp & Parker, 2004) determines the seed point. The region growing finds the ROI by grouping pixels in the surrounding seeds using the probabilistic approach. The study by Shan et al. (2012) ensures complete coverage of the ROI by N-pixel expansion in both vertical and horizontal directions. The procedure ensures that the seed points and all surrounding pixels are encapsulated for growing

Selecting the seeds is one of the open problems in the region growing. Manual seed required a human operator. Automatic seed selection is often based on the gray level, texture, and other features that fail. Among the proposed steps in automatic seed selection are noise reduction, iterative threshold selection (Ridler & Calvard, 1978), generating boundary connected regions, region ranking.

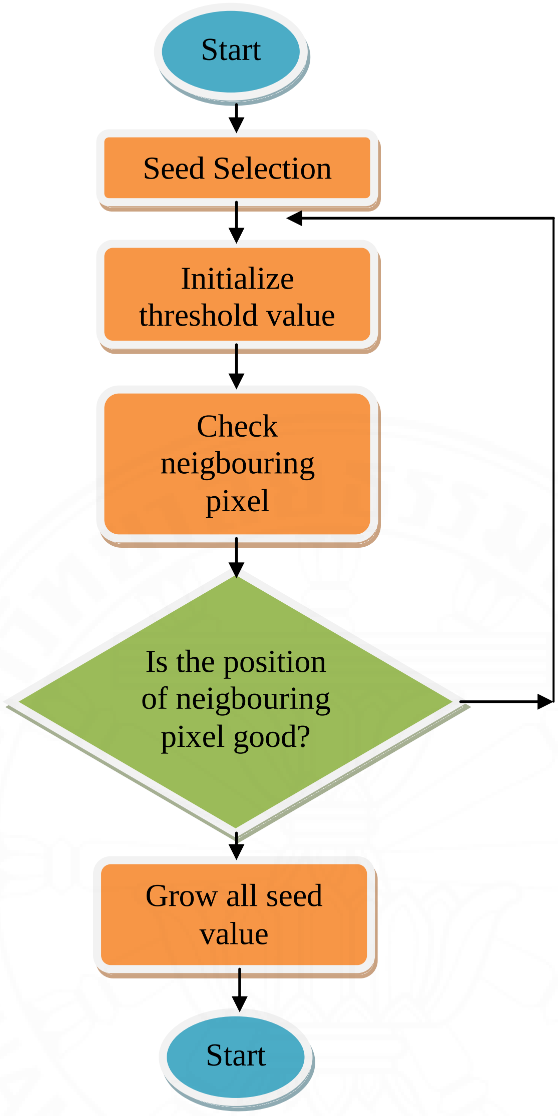

Fig. 7. Flow Chart of region growing algorithm

The watershed transform was introduced by (Digabel & Lantujoul, 1978) for image processing and now is being used as a powerful fundamental step in computer vision and pattern recognition (Cousty et al., 2009). There are several definitions of watershed, however, the most common definition was proposed by Beucher and Meyer (1993). They define watershed as a flooding procedure that places a water source in each regional minimum to cover the entire relief from building barriers when different sources converge. The purpose of watershed transform is to detect lines on the topographic surface, and then flood regions preventing adjacent minimal. The watershed algorithm is used to determine continuous boundaries in an image.

One of the first applications of the watershed to BUS images is Ikedo et al. (2007). They use the combinations of canny edge detector and watershed to segment BUS images. Edges are identified with the canny method, and then the morphological operator classified these edges as near-vertical or near-horizontal. Next, the edge positions are located with a mass candidate and interpreted as a cue for the segmentation method. Finally, the watershed method segment the mass candidate regions.

Gomez et al. (2010) used the marker-controlled watershed algorithm to segment tumors in BUS images. First, the images were enhanced with CLAHE. Then, the anisotropic diffusion filter was used to remove speckle. The complement of the filtered image was convoluted with a Gaussian function. Subsequently, a marker morphological operation function was created. Finally, the watershed algorithm segmented the image. The interesting aspect of this approach was the iterative procedure. This procedure involved gray-level thresholding and a marker-controlled function. Once the marker-controlled function was stable, the gray-level function remained stable.

Zhang et al. (2010) used the fuzzy watershed method to segment BUS images. A fully automatic algorithm that produces good results on blurry BUS images is presented. Huang and Chen (2004) used watershed and active contour models to segment tumors in BUS images. They use the watershed model to automatically identify initial contours and to maintain tumor shape and boundary. Active contour segments the images. Findings from their study show consistency with manual contour identification.

Lo et al. (2014) combine a computer-aided detection system with the watershed algorithm to segment BUS images. The images were divided into five slices with a variation and an overlapping function. Then, the minimum intensity projection was applied to the image. Finally, top-down gradient descent and the watershed method segmented the tumors. Gu et al. (2016) extract edge information from the Sobel operator to obtain a gradient magnitude image. This information is used by the watershed transform. The watershed transforms process the edge information and performs segmentation in the slices and the image is represented as a surface in 3D space.

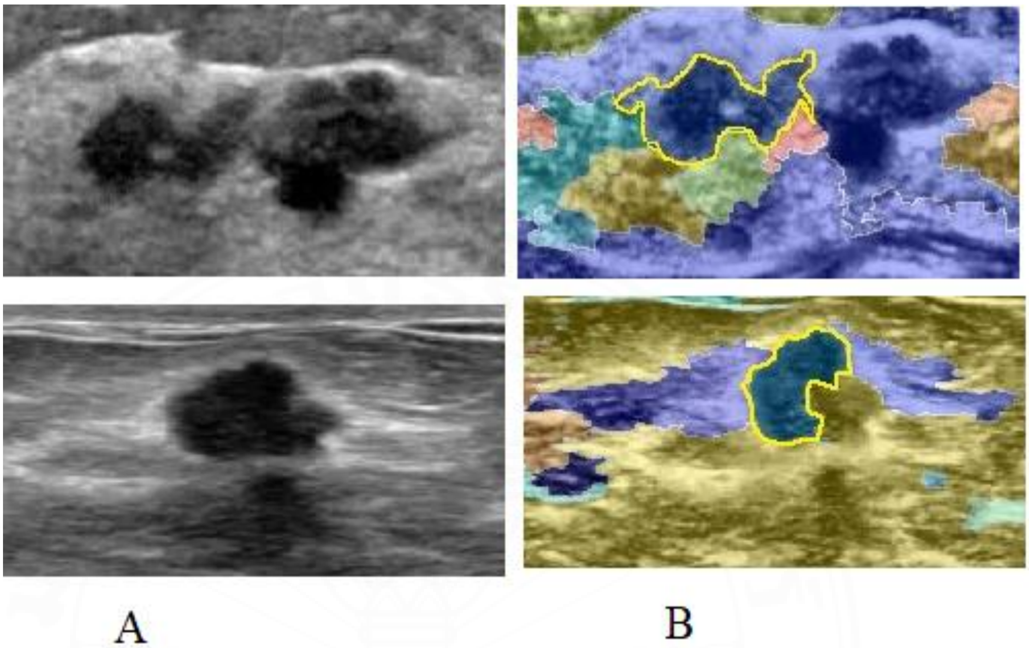

Fig. 8. BUS images with watershed segmentation. (A) Original image, (B) watershed segmentation

The watershed algorithm uses a combination of mathematical morphology theory and simulated terrain surface to segment images. Traditional watershed-based methods are sensitive to noise and are prone to over-segmentation. However, with the development of the marker methods, watershed methods have produced tremendous results. Finally, experiments indicate that the watershed algorithm produces stable results when compared with thresholding and region growing methods (Zhang et al, 2018).

2.3 Superpixel Segmentation

Superpixels group pixels using color and intensity (Yuan et al., 2018). Advantages of superpixels in image processing include reduced computational cost and effective noise removal. The examples are waterpixels (Machairas et al., 2015), density-based spatial clustering (Shen et al., 2016), and Simple Linear Iterative

Clustering (SLIC) (Achanta et al., 2012). Superpixels are popular in medical image processing. Yuan et al. (2018) propose a combination of the random walk, active contours, and superpixels for liver segmentation. Gao et al. (2017) use superpixels as nodes for generating gradient cues and spatial priors. The segmentation procedure uses the graph cut to extract the boundaries from the gradient cues and spatial priors.

Tana et al. (2016), propose a learning phase based on pre-processing and multiscale representation. Subsequently, the SLIC creates superpixels. Features are extracted from the superpixels and are used for classification by the SVM.

Yuan et al. (2018) combine the random walk, active contours, and superpixels for liver segmentation. Superpixels are used for preprocessing. This hybrid segmentation method produced accurate results, however, is prone to over-segmentation. Huang et al. (2020) segment and classifies BUS images using the learning framework. First, the region of interest is cropped out from the original image. Then the image is preprocessed by the bilateral filter, the histogram equalization, and the mean shift filter. Next, SLIC creates superpixels. The features extracted from the superpixels are gray level histogram, Gray Level Co-occurrence Matrix (GLCM), and the local binary pattern (LBP). The K-means algorithm for clustering procedure and a backpropagation neural network (BPNN) are used for initial classification. Finally, the k-nearest neighbor algorithm, binary thresholding, and the edge segmentation method produce the tumor region. Although this method gives a good segmentation result, it fails when the tumors vary in size. The method proposed in this dissertation tackles the above-mentioned drawbacks.

CHAPTER 3
METHODOLOGY

3 Design Method and Procedures

The proposed method includes a pre-processing stage, a segmentation stage depicted in Figs. 9, 10, and 11.

3.1 Pre-processing Stage

We propose a new pre-processing algorithm that removes speckles and artifacts in BUS images. The method is based on a multiscale decomposition, the Wiener filter, fast bilateral filter, and wavelet decomposition combined with the anisotropic filter.

3.1.1 Multiscale

To construct a Laplacian pyramid we use the low pass Gaussian filter $G(t,u,v)=\frac{1}{\sqrt{2\pi t}}\,e^{-(u-v)^2/2t}$ The downsampling procedure is as follows.

$I_1 = I * G \downarrow 2,$

$I_2 = I - I_1 \uparrow 2,$

where $\downarrow 2$ denotes downsampling by 2 and $\uparrow 2$ denotes upsampling by 2. Hence I_1 is the low frequency subband downsampled by 2 (approximation), and I_2 is the high-frequency part.

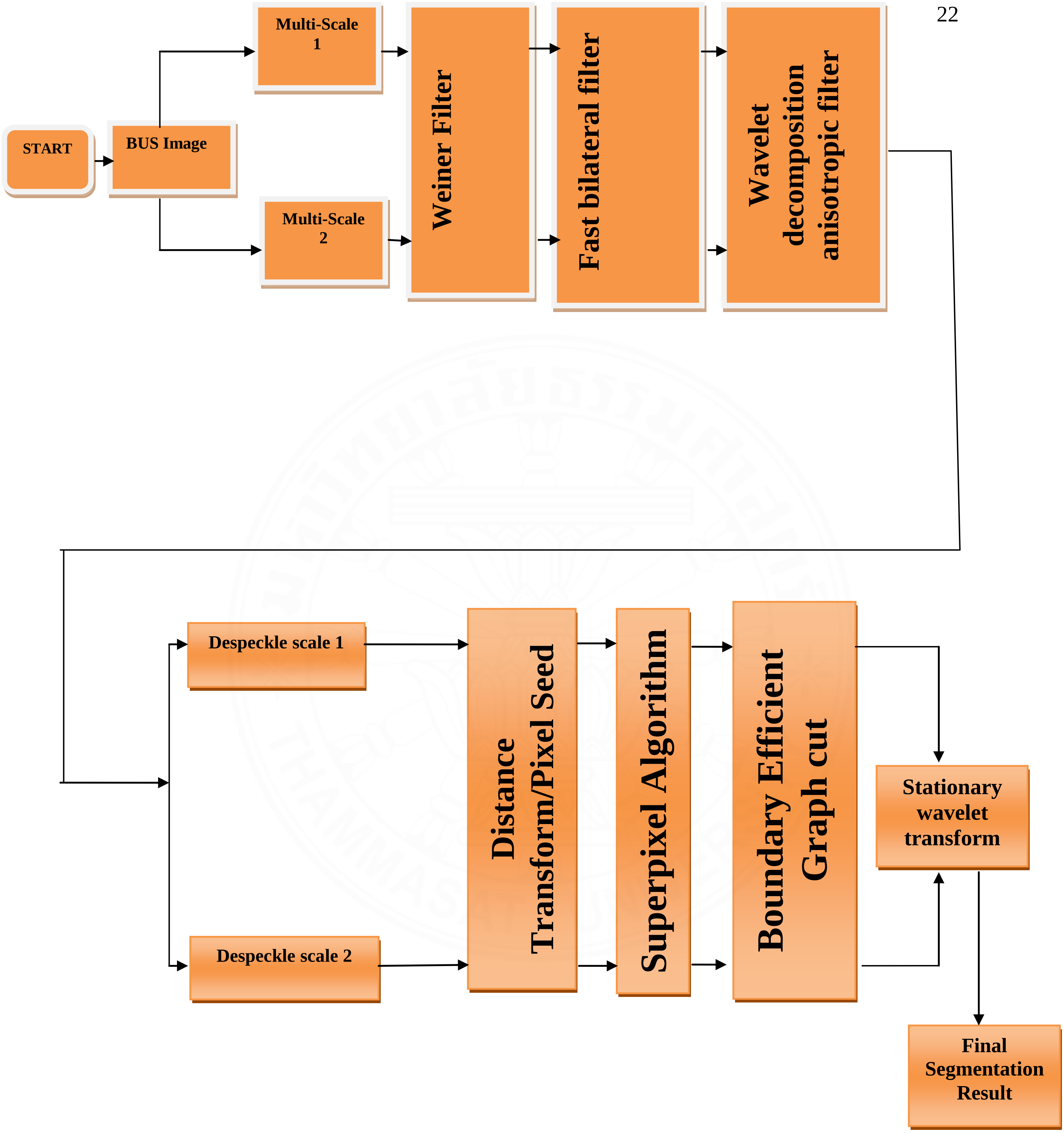

Fig. 9: Proposed Segmentation Block Diagram

I_1 and I_2 have been processed and synthesized, the output can be subjected to the Laplacian pyramid procedure again. Training of subbands and the required subsampling depends on the individual set of images.

3.1.2 Weiner Filter

The adaptive Weiner filter (WF) (Baselice et al., 2018), is designed specifically for speckle noise. The classic WF adapts by tuning its kernel to combine edge and detail preservation. Effective noise reduction is achieved with the local Gaussian Markov random field.

3.1.3 Fast bilateral filter

The conventional bilateral filter (BF) replaces the central pixels with the average of its neighbors to remove noise. Although the BF is effective, it often leads to over-fitting. Images filtered with BF produce blurry edges and artifacts. To improve the efficiency of the BF procedure, and shorten the running time we use a modification of the fast version of the BF (FBF)(Paris & Durand, 2006) based on a three-dimensional Gaussian kernel and image function. The FBF uses a fast Fourier transform and higher-dimensional frequency space to downsample the results of the convolution. A special edge-preserving version of the FBF is used to process the high-frequency component (Jin et al., 2015).

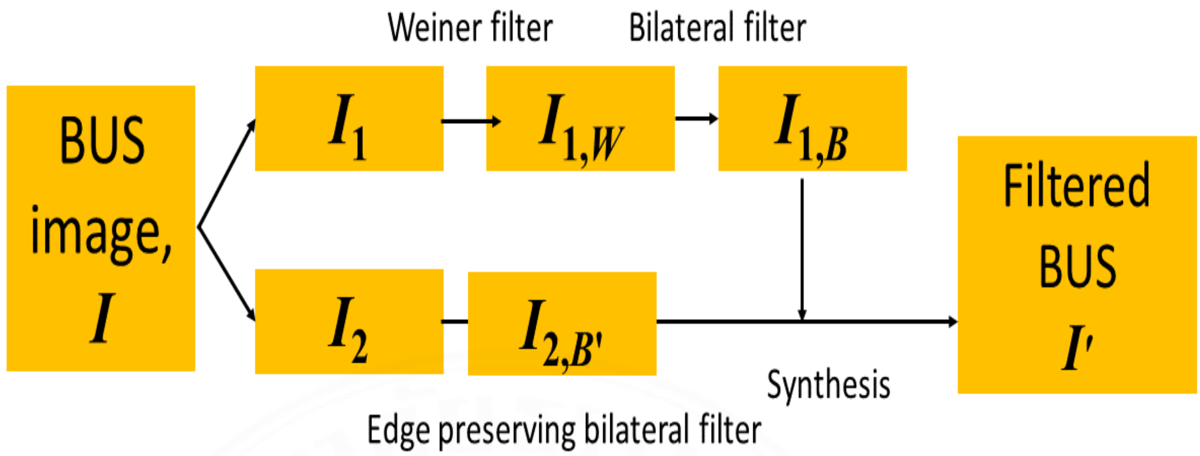

Fig.10. Block diagram of the first stage, $I_{1,w}$- output of the transformation. This Weiner filter, $I_{1,B}$ -output of the BF, $I_{1,B'}$- output of the edge preserving BF

3.1.4 Wavelet decomposition anisotropic filter

The threshold rule is a procedure that performs the wavelet denoising (Donoho & Johnstone, 1994). We use the wavelet decomposition of MATLAB Wavelet Image Denoising Library. The coefficients at the coarse level are being kept whereas the detailed coefficients are removed using the median absolute deviation rule taken as a crude estimate of the noise (see Fig. 11).

3.1.4.1 Anisotropic diffusion

The output of the wavelet denoising is fed to the AD filter, given by

$$\frac{\partial I}{\partial t} = \operatorname{div}(g \nabla I). \tag{1}$$

The classic diffusion coefficients proposed by Perona and Malik are

$$g(\nabla I) = \frac{1}{1 + \left(\frac{\nabla I}{\lambda}\right)^2} \tag{2}$$

and

$$g(\nabla I) = \exp\left(-\left(\frac{\nabla I}{\lambda}\right)^2\right), \tag{3}$$

where λ is an adjustable parameter. Experiments show that due to staircase effect equations (2)-(3) are not suitable for BUS images. Therefore, a new diffusion coefficient is proposed given by,

$$D(Q) = 1 - \frac{1}{1 + \exp(-k(Q^2 - Q_0^2))}, \tag{4}$$

where k is an adjustable parameter and Q_0 is the speckle scale function. Q is the instantaneous coefficient of variation, given by

$$Q = \frac{\frac{1}{2}\left(\frac{|\nabla I|}{I}\right)^2 - \frac{1}{16}\left(\frac{|\nabla^2 I|}{I}\right)^2}{\left(1 + \frac{1}{4}\left(\frac{|\nabla^2 I|}{I}\right)\right)^2} \tag{5}$$

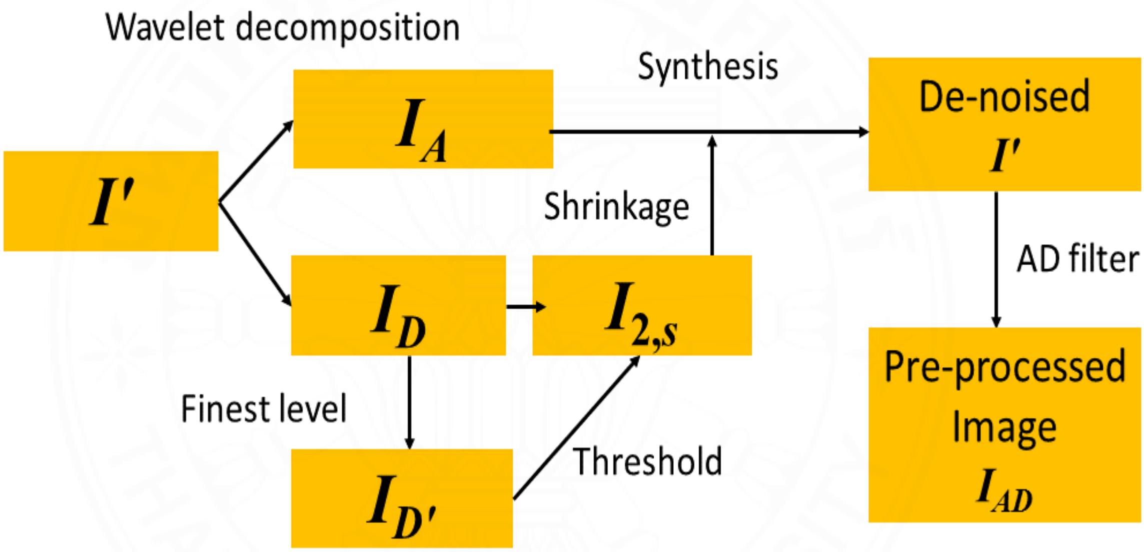

Fig.11. Block diagram of the second stage, I_A- approximation, $I_{1,D}$ -details,$I_{1,D'}$- the finest bands, I_{AD}- output.

3.2 Segmentation Stage

The preprocessed images (3.1) are fed to the segmentation module (see Figs 12 and 13). The components of the segmentation stage are explained below.

3.2.1 Distance Transform/Pixel Seed Measure.

The practical experiments reveal that the SLIC algorithm does not adhere well to large boundaries. To correct this problem, we use the geodesic distance transform to generate a map that adheres equally well to small and large boundaries. First, a brief understanding of the conventional SLIC is required. It involves the color similarity in the labxy space as follows

$$P(O, C_0) = \sqrt{P_c^2(O, C_0) + \gamma^2 P_s{}^2(O, C_0)}\ , \tag{6}$$

where γ is the regulating factors, $(O, C_0\ )$ is the superpixel centre, P_c *and* P_s are colour and spatial distances. The lab colour distance is given by:

$$P_c(O, C_0) = \sqrt{\left(l_0 - l_{C_0}\right)^2 + \left(a_0 - a_{C_0}\right)^2 + \left(b_0 - b_{C_0}\right)^2}\ , \tag{7}$$

The spatial distance is

$$P_s(O, C_0) = \sqrt{\left(x_0 - x_{C_0}\right)^2 + \left(y_0 - y_{C_0}\right)^2}, \tag{8}$$

$P_c(0, C_0)$ and $P_s(0, C_0)$ are the classic Euclidean distances in the color and spatial domains, respectively. Note that for the gray level image $P_c(O, C_0) = |l_0 - l_{C_0}|$.

To improve the SLIC, a new superpixel seed measure is proposed. To create the geodesic segmentation, we convert the grayscale image to a binary image. The modification of equation (6) is:

$$P(O, C_0) = \sqrt{P_c{}^2(O, C_0) + \gamma^2 P_s{}^2(O, C_0) + (\alpha P_b(O, C_0) Geo_{GL}(C_0))^2}, \tag{9}$$

where P_b is the boundary term, α is the distance constant, and Geo is the geodesic distance given by:

$$Geo_{GL}(x^{\rightarrow}) = \min_{y^{\rightarrow} \in \Omega_{GL}} d_{GL}(x^{\rightarrow}, y^{\rightarrow}) + O_L f_L(x^{\rightarrow}, y^{\rightarrow}), \tag{10}$$

where

$$d_{GL}(x^{\rightarrow}, y^{\rightarrow}) = \min_{L_{x^{\rightarrow}, y^{\rightarrow}}} \int_0^1 W_{GL}(L_{x^{\rightarrow}, y^{\rightarrow}}(S))\,.\,L^{\sim}{}_{x^{\rightarrow}, y^{\rightarrow}}(S) dS, \tag{11}$$

and where $L_{x^{\rightarrow}, y^{\rightarrow}}$ is a path parameterized by $S \in |0, 1|$ connecting $x^{\rightarrow}$, to $y^{\rightarrow}$, W_{GL} is the geodesic weight, and $L^{\sim}{}_{x^{\rightarrow}, y^{\rightarrow}}$ is the length of the path (Peng & Qu, 2019).

The boundary term P_b ensures that the centroid of the superpixel does not lie at the boundary of the object. If the gradient of the gray level around O is large, the boundary term is large, otherwise, it is small.

3.2.2 Superpixel algorithm.

The SLIC algorithm is applied to the GD image and a final superpixel image is created (see Fig. 12).

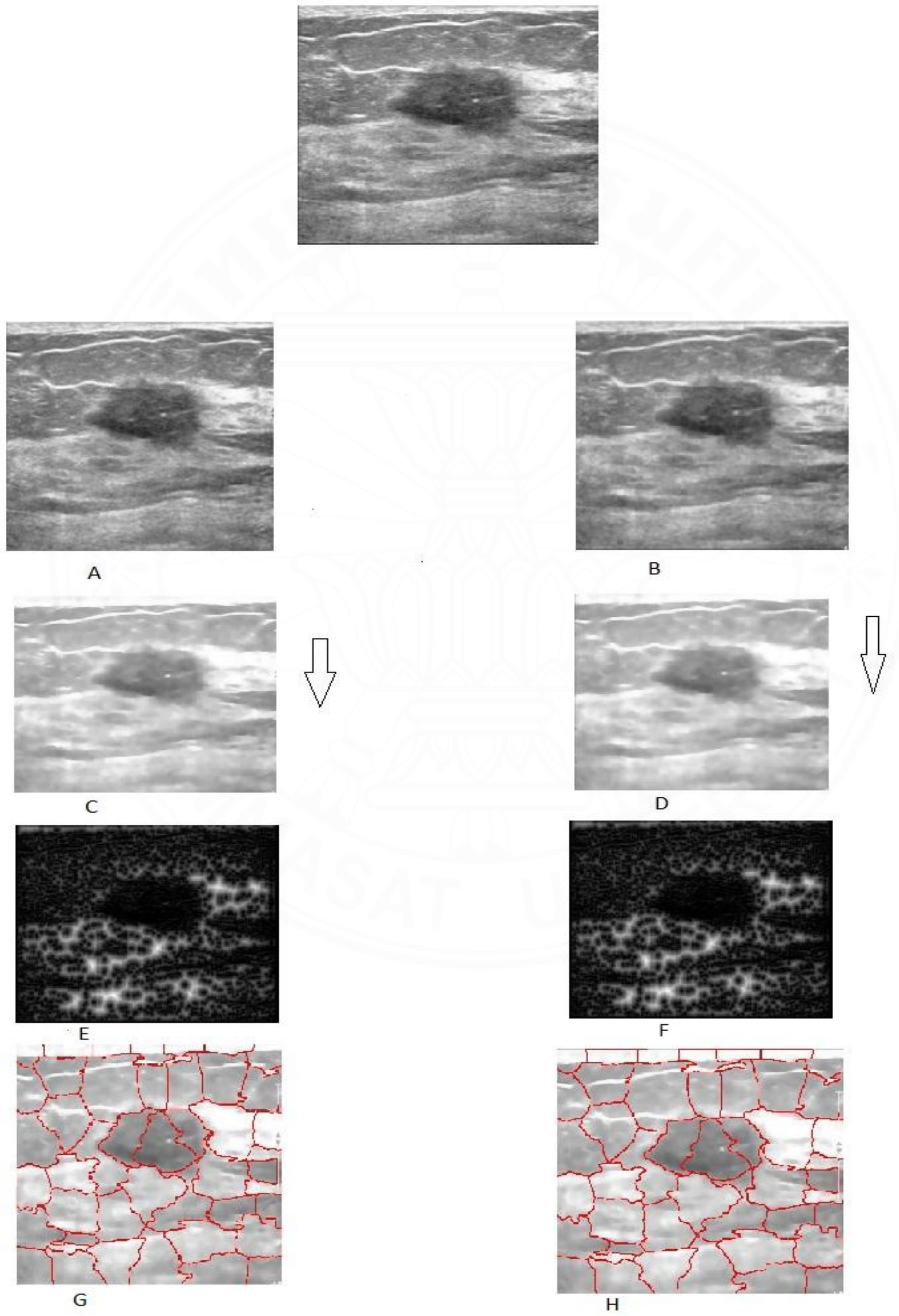

Fig. 12. Proposed superpixel improvement (A) and (B) Multiscale images (C) and (D) Preprocessed images (E) and (F) Decomposition transform (G) and (H) proposed superpixel

3.2.3 Boundary Efficient Graph Cut method

The graph cut method has been adopted over the years for segmenting medical images. Standard methods based on superpixels for segmenting BUS images often result in over-segmentation. To avoid this problem, a symmetry measure combined with the graph cut method is proposed. The graph cut algorithm introduces n-links and t-links. The n-link connects the neighboring pixels while the t-links connect pixels with terminals S and T (Peng, Qu & Li, 2019). The conventional cost of the neighborhood edge (n-link) is given by the following equation:

$$P(r,s) = \mathrm{e}^{-\frac{(Q_r - Q_s)^2}{2\sigma^2}} \frac{1}{||r-s||},\ \{r,s\} \in M\ , \qquad (12)$$

where Q_r and Q_s are the intensity of pixels of r and s, M is a set of neighboring pixels, σ is the empirical value, and || || denotes the Euclidean norm. The use of the distance transform with the graph cut is efficient because both methods work in the same domain. The cost for the terminal edges (t-links) of the graph cut method is defined by:

$$P(r,S) = \begin{cases} k, \text{if } r \in O, \\ O, \text{if } r \in B, \\ -\ln P_r\left(\frac{Q_r}{B}\right), \text{otherwise.} \end{cases} \qquad (13)$$

$$P(r,T) = \begin{cases} k, \text{if } r \in O, \\ O, \text{if } r \in B, \\ -\mathrm{In} P_r\left(\frac{Q_r}{O}\right), \text{otherwise.} \end{cases} , \qquad (14)$$

Note that *O* denotes the object and *B* the background.

$$k = 1 + \max_{V} \sum\nolimits_{s:\{\mathrm{r,s}\}\in M} P(r,s)\ \ , \qquad (15)$$

where $Pr\left(\frac{Q_r}{B}\right)$ and $Pr\left(\frac{Q_r}{O}\right)$ are the normalized histograms. (Zhang, Wang &Shi, 2009). The minimum cost cut for the background and the object is defined by:

$$E = \gamma_t \sum_{r \epsilon P} (P(r,S) + P(r,T)) + \sum_{r \in P, \{r,s\} \epsilon M} P(r,s)\ , \qquad (16)$$

where the first term corresponds to the region and the second to the boundary of the superpixel, γ_t is the weighting factor

Symmetry is an important criterion in medical diagnosis. Several research papers have shown the importance of this feature (Kiryati & Gofman, 1998, Sun, 1995). Therefore, we introduce the mirror symmetry measure (Ng et al., 2005). The tumors are, especially on the low-resolution level and are characterized by a certain level of symmetry. Segmentations with a high level of asymmetry are rejected.

Finally, the discrete stationary wavelet transform is used to fuse the segmentations obtained on different resolution levels (Mu et al., 2018).

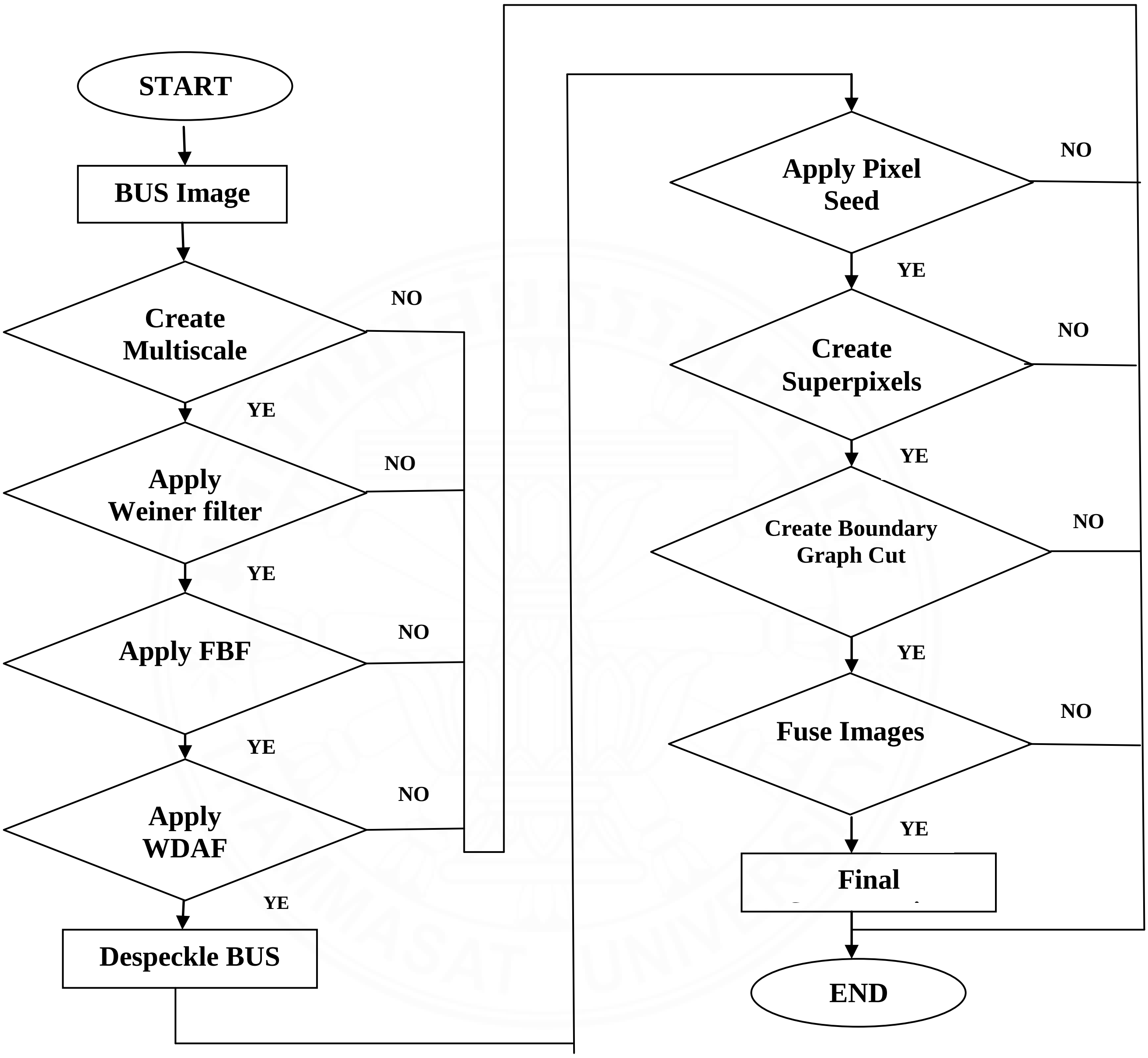

Fig. 13. Flowchart of the proposed method

CHAPTER 4
PRE-PROCESSING

4. Results

The proposed pre-processing algorithm is tested on 50 synthetic images degraded by speckle noise with varying intensity. Further, the method is tested on 250 BUS images from the Thammasat University Hospital database (Rodtooket al., 2018) and Baheya Hospital for Early Detection & Treatment of Women's Cancer (Al-Dhabyani et al., 2020). Different images (50), taken randomly from each database, are used for training.

4.1. Data acquisition and experimental setup

Evaluation of the filters on a set of real images is not a trivial task since the reference images are not available. The performance evaluation can rely on synthetic images or a subjective evaluation by a pool of experts (Shrimali, Anand, &Kumar, 2010). Alternatively, BUS images can be additionally distorted (Ilesanmi, Idowu, & Makhanov, 2020). However, such reference images do not represent the desired result. Finally, there exist several non-reference methods. However, they require reliable statistics regarding the noise. In this pre-processing stage, we use a different approach, applied to non-reference BUS images. Namely, we apply conventional image segmentation methods, e.g., the morphological active contours without edges (Ning, Zhang, &Liao, 2019), the watershed method (Kim, Nam, & Jang, 2018), and the K-means with Otsu thresholding (Harb, Isa,&Salamah, 2015; Jaroša et al., 2017). The results are compared with the ground truth provided by the radiologists. The quality of segmentation is assessed by the DICE, Jaccard coefficients, and the Hausdorff distance which are among the most popular measures of segmentation in medical image processing. Denoising of the synthetic images is evaluated by the standard quality measures such as the mean-square error, the signal-to-noise ratio, the peak signal-to-noise ratio, and the structural similarity index. The experiments are performed on an Intel(R) Dual-Core CPU (3.60 GHz, 16GB RAM), Windows 10.

Consider the following quality measures.

(a) The Mean-Square Error (MSE). The MSE measures the quality between the denoised image and the original image. Lower values of the MSE indicate better quality of the denoised image (Sudeep et al., 2015).

$$\text{MSE} = \frac{1}{N}||I - L||^2, \tag{17}$$

where I is the original image, L is the denoised image, N is the number of data points, and || || is the Euclidean norm.

(b) The Signal-to-Noise ratio (SNR) measures the level of noise relative to the original image as follows.

$$\text{SNR} = 10\log_{10}\frac{||L||}{||\text{I} - \text{L}||}, \tag{18}$$

where L is the reference image and I is the denoised image.

(c) The Structural Similarity Index Measure (SSIM) is given by

$$\text{SSIM}(u, v) = \frac{(2\mu_I\mu_L + Q_1)(2\sigma_{IL} + Q_2)}{({\mu_I}^2 + {\mu_L}^2 + Q_1)({\sigma_I}^2 + {\sigma_L}^2 + Q_2)}, \tag{19}$$

where μ_I and μ_L are the average gray values, σ_I and σ_L are the variance of patches, σ_{IL} is the covariance of *I* and *L*, and Q_1 and Q_2 denote two small positive constants (typically 0.01).

(d) The Peak Signal-to-Noise Ratio (PSNR) measures the ratio between the maximum original signal and the MSE.

$$\text{PSNR} = 10 * \log_{10}\left(\frac{(\max(I))^2}{MSE}\right). \tag{20}$$

(e) The Jaccard Similarity Coefficient (JSC), used to evaluate the quality of segmentation, is given by

$$JSC(B, B_{GT}) = \frac{|B \cap B_{GT}|}{|B \cup B_{GT}|}, \tag{21}$$

where B and B_{GT} stand for the segmented object and the ground truth.

(f) The Dice Similarity Coefficient (DSC) is a measure that is similar to the JSC, given by

$$DSC(B, B_{GT}) = 2\frac{|B \cap B_{GT}|}{|B| + |B_{GT}|}. \tag{22}$$

(h) The contour-based Hausdorff distance (HD) is given by

$$\text{dist}_H(X, Y) = \max\{\max_{a\in X}\min_{b\in Y}||a - b||, \max_{b\in Y}\min_{a\in X}||a - b||\}, \tag{23}$$

where X is the ground truth contour and Y is the resulting contour.

4.2 Experiment 1: pre-processing of synthetic images

Fifty synthetic images degraded by the speckle noise have been subjected to the prescribed filters. The SNR is in the range [2.07, 12.34]. The conventional filters, such as the MF, BF, WF, SRAD, etc. constitute the first set (Table 1, clear cells). The second set includes the speckle reduction filters (shaded cells Table 1)

Table 1: Noise reduction algorithms

Filter	Reference	Remark	Availability
MF	(Zhu &Huang, 2012)	Nonlinear	Downloadable code
BF	(Omasi &Manduchi, 2006)	statistical, locally adaptive	Downloadable code
WF	(Pratt,1972)	statistical, locally adaptive	Downloadable code
(SRAD)	(Can-Fei, et al., 2012)	iterative	Downloadable code
Guided Filter (GF)	(He, Sun, &Tang, 2010)	locally adaptive	Downloadable code
Fast BF (FBF)	(Paris,& Durand,2006)	iterative	Downloadable code
Anisotropic Diffusion Memory Speckle Statistics (ADMSS)	(Ramos-Llordén et al., 2015)	locally adaptive	Downloadable code
Fast Bilateral Filtering Fourier Kernel (FBFFK)	(Ghosh& Chaudhary,2016)	locally adaptive	Downloadable code
Discrete Topological Derivative (DTD)	(Damodaranet al., 2012)	locally adaptive	Downloadable code
Combination Spatial Filtering (CSF)	(Garg &Khandelwal, 2018)	hybrid	Implemented by the authors
Hybrid Speckle Reduction Filter(HSRF)	(Singh et al., 2017)	hybrid	Implemented by the authors
Multi-scale hybrid method (MSHM)	Proposed	hybrid	Implemented by the authors

Finally, the third set is the hybrid filters, CSF and HSRF (shaded red cells Table 1). Tables 2-3 show the efficiency of the MSHM (proposed pre-processing method) relative to the reference methods.

Table 2: Efficiency of the proposed filter applied to synthetic images, MSE and SNR

Filter/Quality	**Average MSE**				**Average SNR**			
Raw noisy image	148.82	153.39	169.48	180.21	12.34	6.62	2.94	2.07
MF	132.40	141.73	160.44	174.38	15.96	9.86	5.36	4.89
BF	117.03	137.42	152.83	168.30	18.42	12.34	8.28	7.42
WF	129.43	140.82	160.03	172.36	16.96	10.78	6.49	5.82
SRAD	127.02	140.66	158.34	170.43	20.42	14.04	10.62	9.44
GF	131.44	141.02	160.22	171.08	16.02	10.40	6.22	5.43
FBF	115.30	121.22	144.02	150.42	21.73	15.60	11.40	10.22
ADMSS	98.89	120.66	132.94	149.07	23.71	17.65	13.07	12.02
FBFFK	97.80	115.94	130.58	148.60	22.04	16.01	11.94	10.95
DTD	83.80	110.10	122.23	138.82	26.43	20.20	16.88	15.43
CSF	79.43	102.21	115.42	130.31	28.81	22.14	18.08	17.31
HSRF	76.62	95.42	108.31	122.41	37.62	30.41	27.10	26.43
MSHM	71.75	88.28	98.99	114.39	41.82	35.21	31.62	30.33

Table 3: Efficiency of the proposed filter applied to synthetic images, SSIM and PSNR.

Filter/Quality	**Average PSNR**				**Average SSIM**			
Raw noisy image	17.43	16.62	14.34	13.06	0.21	0.14	0.11	0.09
MF	21.22	19.68	18.98	18.56	0.41	0.32	0.22	0.19
BF	22.51	20.15	19.02	18.89	0.65	0.58	0.52	0.46
WF	19.02	18.78	17.77	17.41	0.52	0.45	0.32	0.27
SRAD	23.21	21.74	20.51	19.30	0.74	0.62	0.57	0.49
GF	20.42	19.06	18.42	18.02	0.45	0.36	0.29	0.23
FBF	25.61	23.12	21.17	20.01	0.79	0.68	0.62	0.53
ADMSS	26.79	24.21	22.74	21.09	0.81	0.72	0.64	0.57
FBFFK	24.22	22.10	20.77	19.75	0.78	0.65	0.60	0.51
DTD	27.51	25.63	23.10	21.71	0.83	0.77	0.71	0.65
CSF	27.98	26.02	23.79	22.10	0.82	0.73	0.69	0.63
HSRF	28.78	26.51	24.10	23.87	0.86	0.79	0.74	0.68
MSHM	30.81	27.98	25.62	25.02	0.89	0.82	0.77	0.72

Note that the proposed approach outperforms the reference methods, in terms of the SNR and MSE. However, DTD, CSF, and the HSRF show close results in terms of PSNR and SSIM. Fig. 14 shows an example of the synthetic image. The shape of the object and the background of the image are similar to those present in the BUS images.

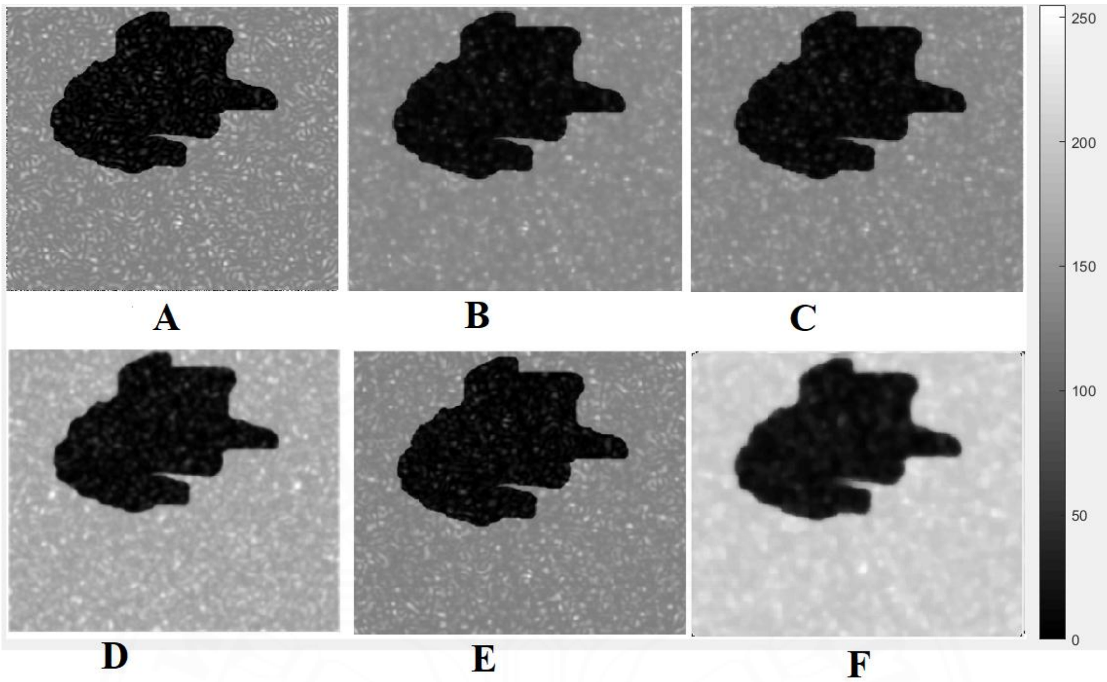

Fig. 14. Speckle-noise filtering for a sample image (A)Noisy image, (B)BF (the best from set 1), (C) DTD (the best from set 2), (D) HSRF (the best from set 3), (E) MF (the worst filter), (F) MSHM (the proposed filter).

4.3 Experiment 2: breast ultrasound images, Thammasat University database

The experiment tests the efficiency of the MSHM on BUS images produced by a Philips iU22 machine from the Thammasat University database, http://onlinemedicalimages.com. The images are preprocessed by the reference filters and segmented using selected conventional segmentation methods, i.e., the morphological active contours, the watershed algorithm, and the K-means with Otsu thresholding.

The results evaluated by the segmentation metrics JSC, DSC, and HD are given in Tables 4-6. The metrics have been averaged over 250 test images. The standard deviation is given. The testing approach avoids the problem of the reference image. It finds the most suitable filters designed specifically for segmentation of the BUS images. Figures 15 and 16 are examples of segmentation of the pre-processed images. To compare with the conventional filters, the best result from the three conventional segmentations was selected for each filter.

Table 4: Segmentation by morphological active contours, Thammasat University database

Filter/Quality	JSC	DSC	HD
MF	0.53±0.19	0.70±0.21	3.77 ± 0.19
BF	0.56±0.21	0.72±0.19	3.79 ± 0.19
WF	0.56±0.36	0.72±0.16	3.73 ± 0.17
SRAD	0.63±0.16	0.78±0.16	3.02 ± 0.16
GF	0.55±0.19	0.71±0.18	3.99 ± 0.17
FBF	0.68± 0.16	0.81± 0.16	2.90± 0.17
ADMSS	0.68± 0.15	0.81± 0.14	2.99 ± 0.18
FBFFK	0.63±0.17	0.78± 0.19	2.85 ± 0.16
DTD	0.68± 0.16	0.81± 0.15	2.63 ± 0.16
CSF	0.69± 0.34	0.82± 0.13	2.54 ± 0.15
HSRF	0.75± 0.14	0.86± 0.12	2.23 ± 0.15
MSHM	0.78± 0.12	0.88± 0.10	2.09 ± 0.11

Table 5: Segmentation by the watershed method, Thammasat University database

Filter/Quality	JSC	DSC	HD
MF	0.57± 0.19	0.73± 0.17	3.92 ± 0.26
BF	0.58± 0.18	0.74± 0.18	3.98 ± 0.23
WF	0.57± 0.18	0.73± 0.19	3.84 ± 0.23
SRAD	0.61± 0.17	0.76± 0.16	2.89 ± 0.19
GF	0.57± 0.19	0.73± 0.18	3.93 ± 0.25
FBF	0.62± 0.19	0.77± 0.15	2.90 ± 0.19
ADMSS	0.63± 0.14	0.78± 0.16	2.95 ± 0.19
FBFFK	0.65± 0.15	0.79± 0.16	2.54 ± 0.17
DTD	0.65± 0.17	0.79± 0.19	2.63 ± 0.16
CSF	0.66± 0.16	0.80± 0.15	2.43 ± 0.16
HSRF	0.72± 0.13	0.84± 0.15	2.15 ± 0.14
MSHM	0.76± 0.10	0.87± 0.11	2.10 ± 0.12

Table 6: Segmentation by K-means with Otsu thresholding, Thammasat University database

Filter/Quality	JSC	DSC	HD
MF	0.65± 0.18	0.79± 0.19	3.80 ± 0.19
BF	0.63± 0.18	0.78± 0.17	3.88 ± 0.20
WF	0.65± 0.17	0.79± 0.19	3.85 ± 0.19
SRAD	0.69± 0.17	0.82± 0.15	3.12 ± 0.16
GF	0.63± 0.18	0.78± 0.20	3.78 ± 0.20
FBF	0.70± 0.17	0.83± 0.16	3.10 ± 0.19
ADMSS	0.72± 0.16	0.84± 0.15	3.08 ± 0.18
FBFFK	0.70± 0.16	0.83± 0.14	3.04 ± 0.18
DTD	0.75± 0.19	0.85± 0.17	2.93 ± 0.14
CSF	0.73± 0.17	0.85± 0.16	2.89 ± 0.17
HSRF	0.76± 0.14	0.87± 0.13	2.65 ± 0.14

MSHM	0.80± 0.13	0.89± 0.12	2.40 ± 0.13

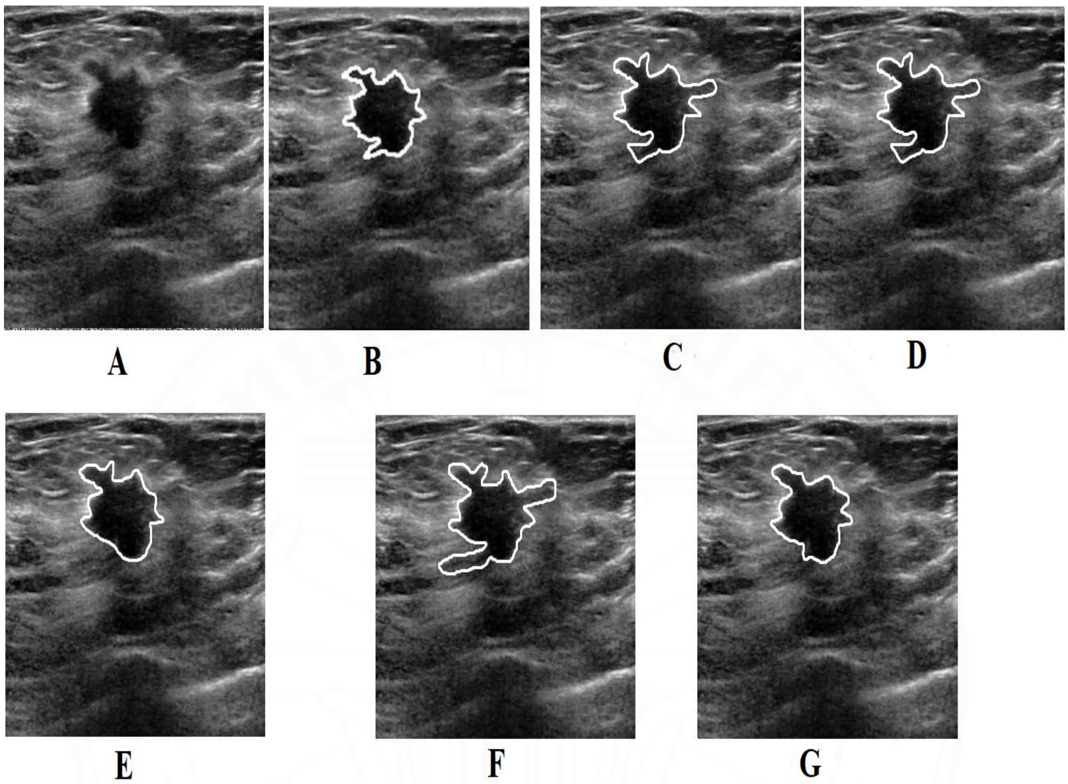

Fig. 15. Segmentation of the pre-processed images (A) Original image, (B) Ground truth, (C) BF(the best from set 1, DSC =0.78), (D) DTD (the best from set 2, DSC =0.80), (E) HSRF (the best from set 3, DSC =0.83),
(F) GF (the worst filer, DSC =0.71), (G)MSHM (DSC =0.86)

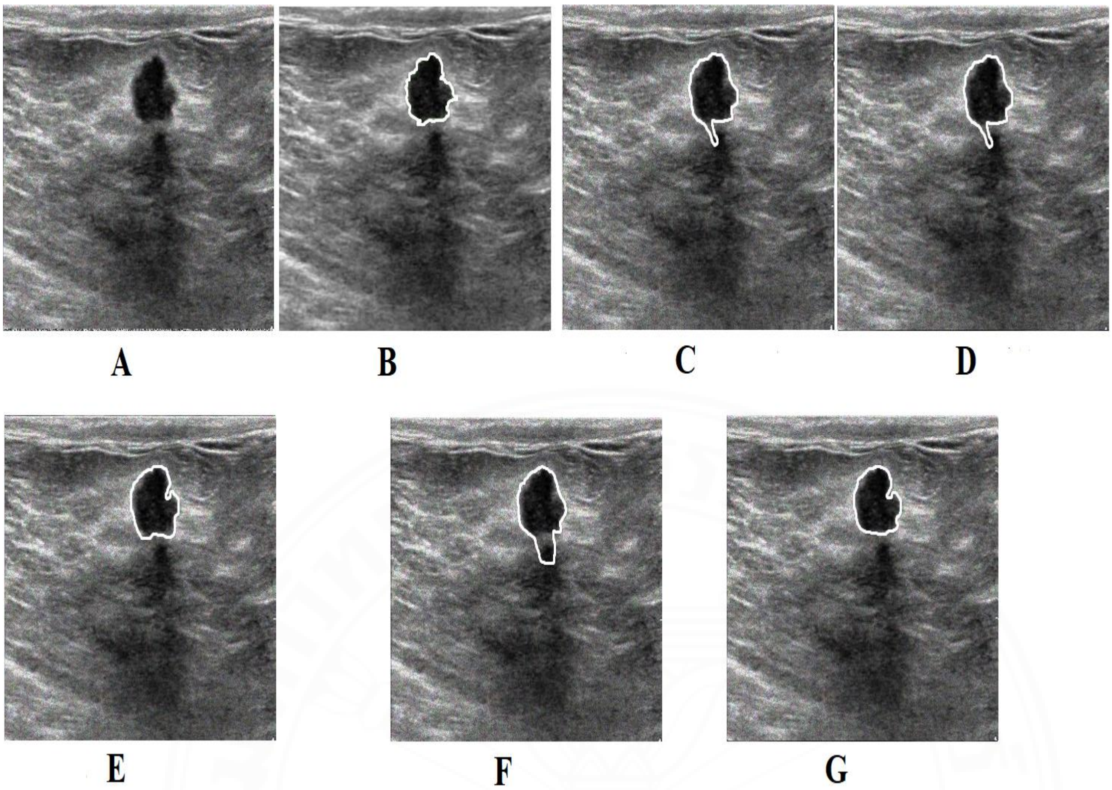

Fig.16. Segmentation of the pre-processed images (A) Original image, (B) Ground truth, (C) BF(the best from set 1, DSC =0.82), (D) DTD (the best from set 2, DSC =0.82), (E) HSRF (the best from set 3, DSC =0.87), (F) GF(the worst filter, DSC =0.76), (G)MSHM (DSC =0.89)

Note that the most popular region-based metrics in validating medical segmentations are the Dice coefficient and the Jaccard index (Taha, & Hanbury, 2015). Several authors suggest that US image segmentation is acceptable if DICE$\geq$0.8 (Hosch, et al., 2002). Tables 4-6, show that only CSF, HSRF, and the proposed method produce acceptable segmentation results, whereas other methods show a substandard performance.

4.4 Experiment 3: Database of Baheya Hospital for Early Detection & Treatment of Women's Cancer

The BUS images are obtained from LOGIQ E9 and LOGIQ E9 Agile machines of the Baheya Hospital for Early Detection & Treatment of Women's Cancer (several hospitals). The ground truth contours have been drawn by experienced radiologists. The efficiency of the proposed method is demonstrated by Tables 7-9 and illustrated in Figs. 15 and 16.

Table 7: Segmentation by the morphological active contours, Baheya Hospital database

Filter/Quality	JSC	DSC	Hausdorff distance
MF	0.56± 0.24	0.72± 0.19	3.20 ± 0.18
BF	0.57± 0.21	0.73± 0.18	3.32 ± 0.18
WF	0.56± 0.20	0.72± 0.18	3.35 ± 0.18
SRAD	0.61± 0.21	0.76± 0.16	2.92 ± 0.16
GF	0.55± 0.23	0.71± 0.20	3.28 ± 0.19
FBF	0.62± 0.22	0.77± 0.17	2.90 ± 0.16
ADMSS	0.63± 0.18	0.78± 0.16	2.88 ± 0.15
FBFFK	0.63± 0.21	0.78± 0.15	2.84 ± 0.16
DTD	0.63± 0.23	0.78± 0.16	2.70 ± 0.15
CSF	0.66± 0.22	0.80± 0.15	2.30 ± 0.14
HSRF	0.68± 0.21	0.81± 0.14	2.15 ± 0.13
MSHM	0.73± 0.17	0.85± 0.12	2.09 ± 0.11

Table 8: Segmentation by the watershed method, Baheya Hospital database

Filter	JSC	DSC	Hausdorff distance
MF	0.60± 0.19	0.75± 0.18	2.97 ± 0.19
BF	0.60± 0.19	0.75± 0.18	2.92 ± 0.19
WF	0.59± 0.20	0.74± 0.19	2.95 ± 0.18
SRAD	0.65± 0.16	0.79± 0.15	2.62 ± 0.15
GF	0.59± 0.19	0.74± 0.19	2.98 ± 0.19
FBF	0.65± 0.16	0.79± 0.17	2.63 ± 0.16
ADMSS	0.63± 0.17	0.78± 0.16	2.68 ± 0.17
FBFFK	0.65± 0.15	0.79± 0.16	2.59 ± 0.16
DTD	0.69± 0.13	0.82± 0.13	2.49 ± 0.14
CSF	0.68± 0.15	0.81± 0.13	2.43 ± 0.13
HSRF	0.72± 0.14	0.84± 0.12	2.29 ± 0.14
MSHM	0.78± 0.10	0.88± 0.09	2.12 ± 0.11

Table 9: Segmentation by the K-means with Otsu thresholding, Baheya Hospital database

Filter	JSC	DSC	Hausdorff distance
MF	0.55± 0.19	0.71± 0.20	2.86 ± 0.19
BF	0.55± 0.19	0.71± 0.18	2.86 ± 0.19

WF	0.56± 0.17	0.72± 0.19	2.88 ± 0.18
SRAD	0.62± 0.16	0.77± 0.18	2.60 ± 0.17
GF	0.52± 0.19	0.72± 0.19	2.83 ± 0.19
FBF	0.62± 0.16	0.77± 0.17	2.60 ± 0.17
ADMSS	0.62± 0.17	0.77± 0.17	2.60 ± 0.17
FBFFK	0.63± 0.16	0.78± 0.17	2.57 ± 0.17
DTD	0.63± 0.15	0.78± 0.16	2.57 ± 0.17
CSF	0.66± 0.15	0.80± 0.15	2.42 ± 0.15
HSRF	0.68± 0.15	0.81± 0.15	2.40 ± 0.14
MSHM	0.69± 0.12	0.87± 0.10	2.03 ± 0.11

In Tables 7-9, CSF, HSRF, and the proposed method produce acceptable segmentation results; whereas other methods show substandard performance (see Fig. 17).

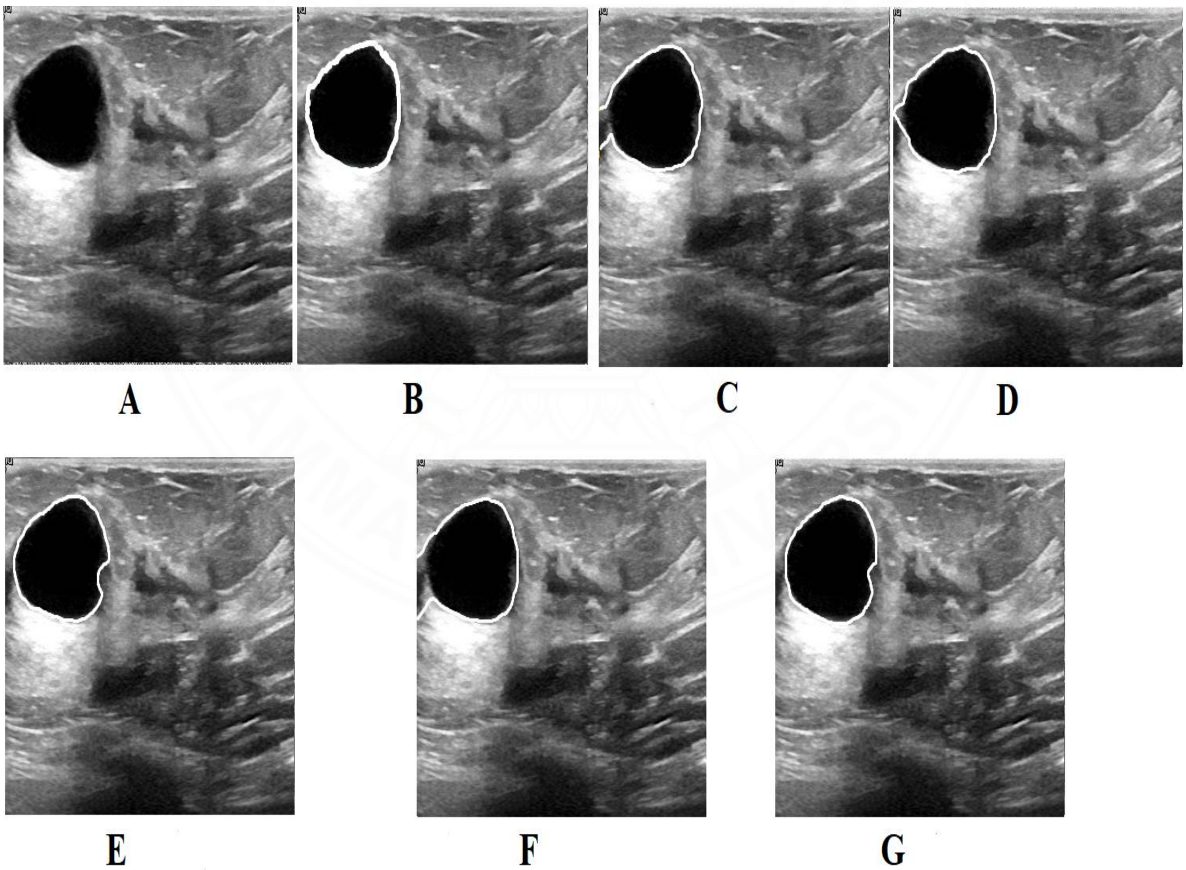

Fig.17. Segmentation of the pre-processed images(A) Original image, (B) Ground truth, (C) BF(the best from set 1, DSC =0.82), (D) DTD (the best from set 2, DSC =0.85), (E) HSRF (the best from set 3, DSC =0.90), (F) GF(the worst filter, DSC =0.78), (G)MSHM (DSC =0.92)

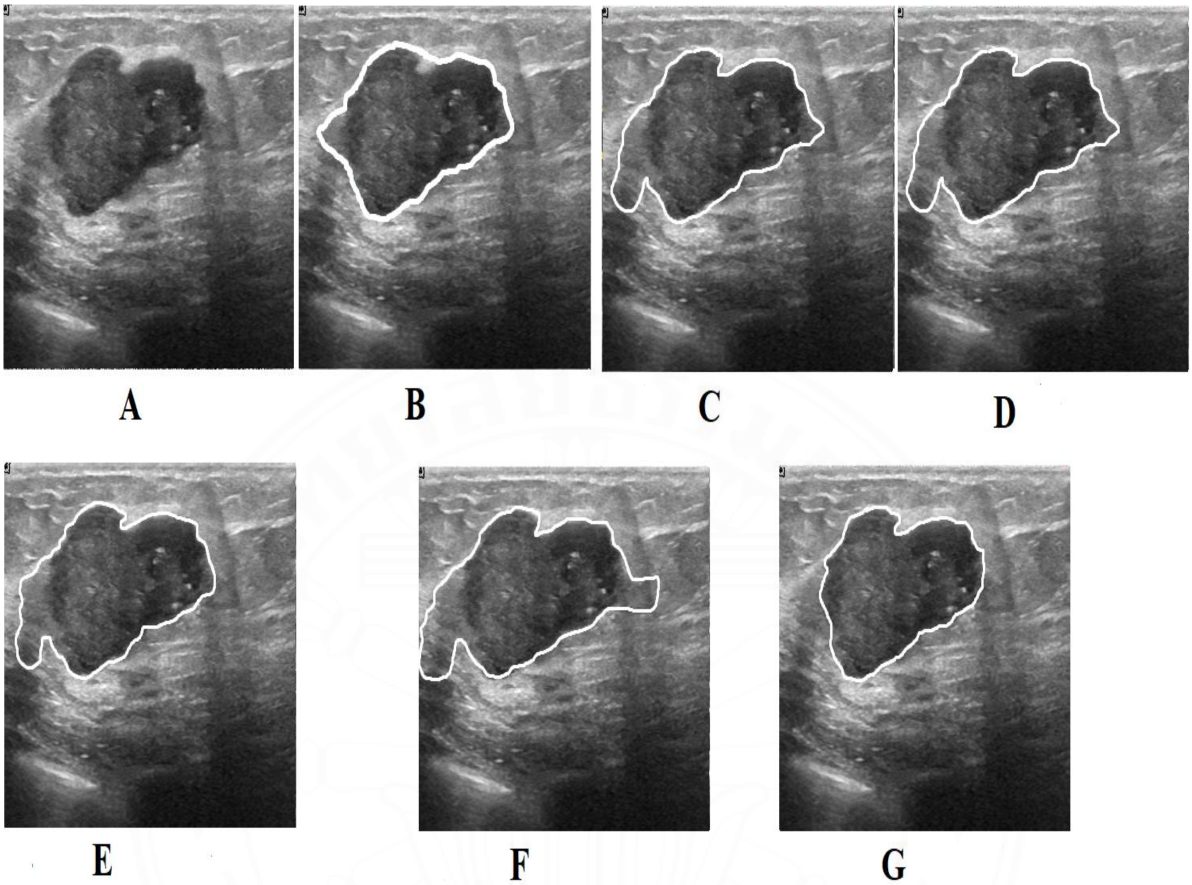

Fig.18. Segmentation of the pre-processed images (A) Original image, (B) Ground truth, (C) BF(the best from set 1, DSC =0.72), (D) DTD (the best from set 2, DSC =0.72), (E) HSRF (the best from set 3, DSC =0.74), (F) GF(the worst filter, DSC =0.70), (G)MSHM (DSC =0.86)

4.5 Discussion: Pre-processing

The pre-processing algorithm has been tested by 250 BUS images from the Thammasat University Hospital database and the Baheya Hospital for Early Detection & Treatment of Women's Cancer database. Additionally, 50 synthetic images corrupted by the speckle noise have been used to test the algorithm. For the synthetic images, the method improves the SNR by 28.7%, PSNR by 11.9%, MSE by 69.6%, and SSIM by 66.25%. The best result of the reference methods is the reduction of the SNR by 25.82%, PSNR by 9.11%, MSE by 58.88%, and SSIM by 51%. Therefore, the improvement concerning the best conventional method is as follows: MSE is 30.31%, SNR is 8.75%, PSNR is 7.12% and SSIM is 51.3%. The improvement relative to the worst conventional result is as follows: MSE is 10.74%, SNR is 3.03%, PSNR is 2.88% and SSIM is 15.3%.

As far as the BUS images are concerned, the improvement achieved by MSHM with regard to the best result of the conventional methods is DSC 8.5%, JSC 11%, and HD 6.7%. The improvement concerning the worst result is DSC 14%, JSC 19%, and HD 13.3%. The DSC and JSC obtained by the proposed algorithm reach the quality standards of medical practice (See Figs 19 and 20). Finally, this testing has been performed only on the unseen images, i.e., the thresholds and other parameters of the procedures have been obtained using different image datasets. This is related to the synthetic and BUS images.

Figs. 22 and 23 summarize the results of the experiments. Overall, the WF and the GF (guided filter) produce the worst results, while the proposed method has the best results for both experiments.

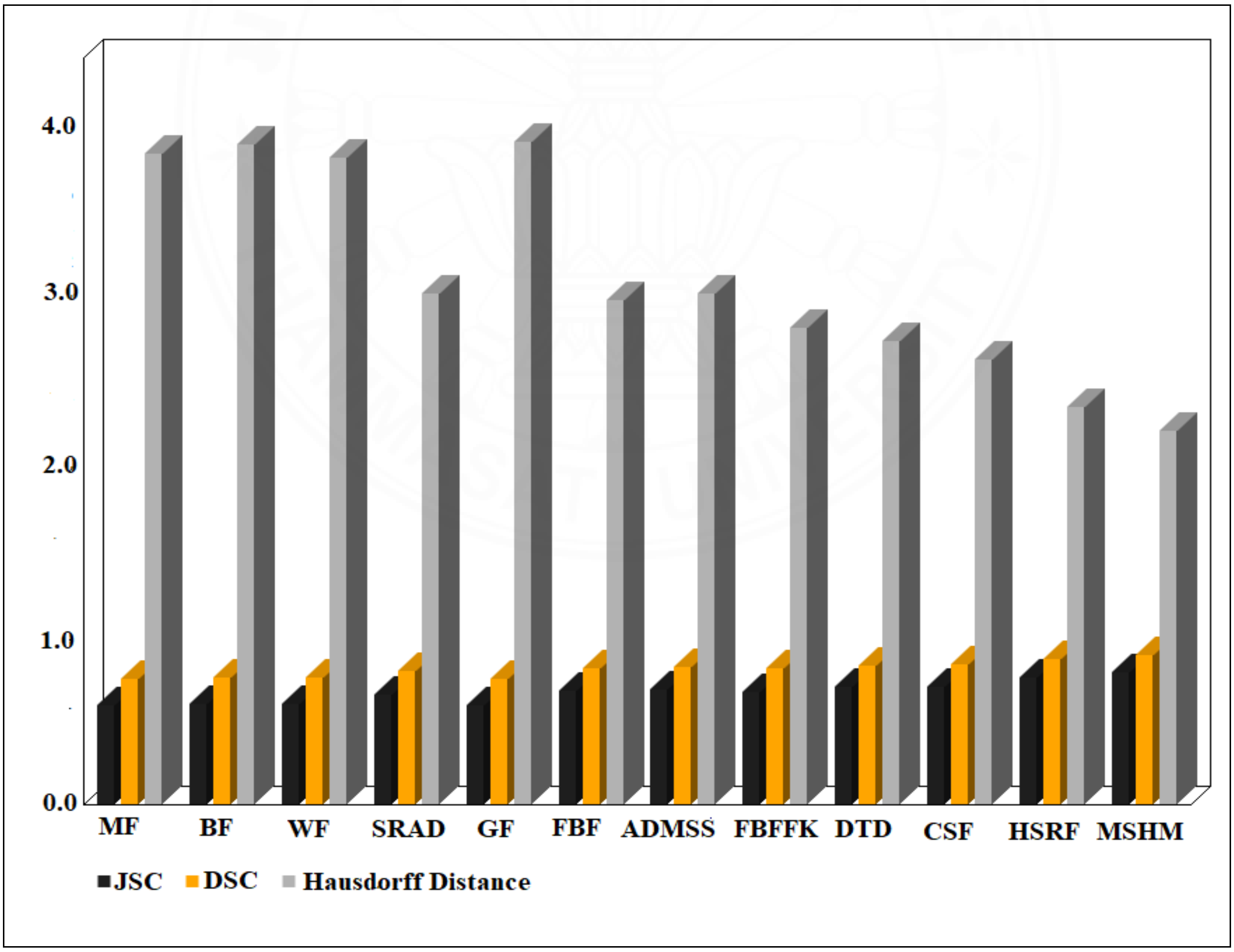

Fig. 19. The efficiency of the methods, Thammasat University database

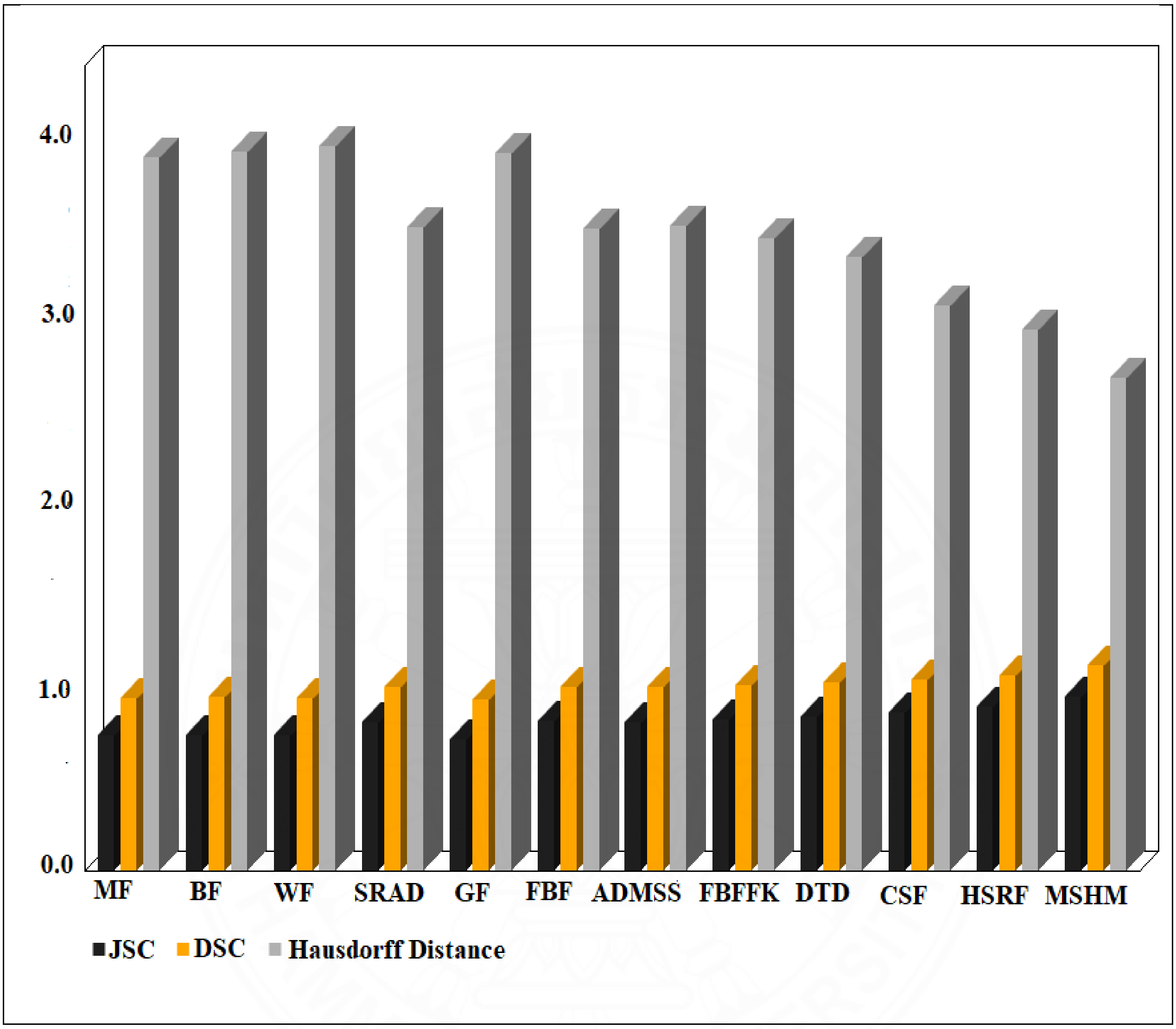

Fig. 20. The efficiency of the methods, Baheya Hospital database.

CHAPTER 5
NUMERICAL RESULTS

5. Results

The segmentations are implemented on Matlab R2018a with an Intel(R) 3.60 GHz CPU, 16GB of RAM, and a Windows 10 Operating System. The average computational time is 0.52s. Four types of BUS images have been considered. Case 1 benign tumors, Case 2 malignant tumors, Case 3 cysts, and Case 4 fibroadenomas.

BUS images have unique and specific features that present difficulty for segmenting. For example, the malignant tumor has an irregular shape making it difficult to segment. The fibroadenoma is characterized by low contrast. Although cysts have a regular shape they are often attached to irregular shadows (fig. 21).

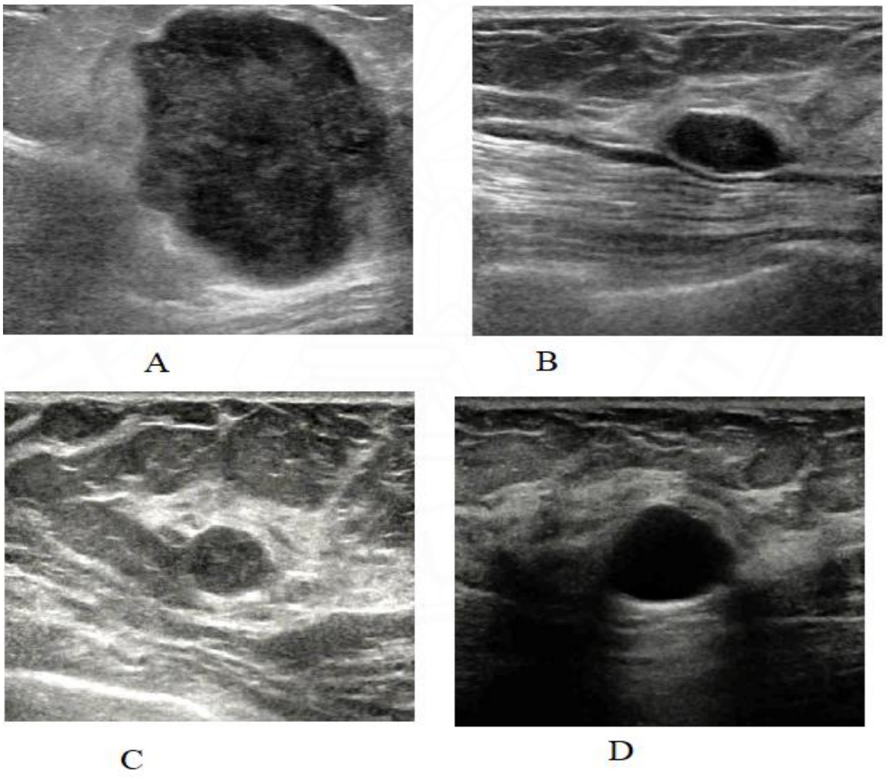

Fig. 21. BUS image Tumour types. (A) Malignant, (B) Benign, (C) Fibroadenoma, (D) Cyst

5.1 Performance evaluation measures

The proposed approach is evaluated on BUS images with the ground truth. The following evaluation measures have been used.

A. Accuracy is the ratio of the true predictions versus the total number of examined cases (Taha, & Hanbury, 2015).

$$ACCURACY = \frac{TP + TN}{P + N}\ , \qquad (24)$$

where *TP*, *TN*, *P*, and *N* stand for the numbers of true positive, true negative, total positive, and total negative samples, respectively.

B. Sensitivity is the ratio of the number of true positives versus the sum of the numbers of true positives and false negatives:

$$SENSITIVITY = \frac{TP}{TP + FN}\ . \qquad (25)$$

C. Specificity is the ratio of the number of true negatives versus the sum of the numbers of true negatives and false positives among the examined cases (Zhou et al., 2016):

$$SPECIFICITY = \frac{TN}{TN + FP}. \qquad (26)$$

D. Precision is the ratio of the number of true positives versus the total number of positive cases among the examined cases (Zhou et al., 2016):

$$PRECISION = \frac{TP}{TP + FP}. \qquad (27)$$

5.2: Results of segmentation of BUS images.

The proposed segmentation method is benchmarked against five methods (CBGC (cell-based graph cut) (Chiang et .al, 2010), ACWE (active contour without edges) (Chan &Vese, 2001), CL (computerized lesion segmentation) (Gomez et al, 2010), ROTM (robust OTU thresholding method) (Sha et al., 2016), and CM (cellular automata method) (Liu et al., 2011)). In addition, four methods from the above benchmarked methods are multiscaled (Multiscale CBGC, Multiscale CL, Multiscale ROTM, and Multiscale CM) and used as the competing methods (see Tables 10 - 14, figs 22 -25). In addition, the proposed preprocessing procedure is used by all methods. The results section is divided into experiments on BUS images not degraded by Gaussian noise (section 5.2), and BUS images degraded by Gaussian noise (section 5.3).

Table 10
Overall result for quantitative evaluations and shape similarity for the proposed and reference methods (**Mean** ± **Standard Deviation**)

Algorithm	**Hausdorff Distance**	**JSC**	**DSC**
CBGC (Chiang et., 2010)	2.512 ± 1.89	0.87 ± 0.72	0.85 ± 0.69
ACWE (Chan &Vese, 2001)	2.419 ± 1.56	0.92 ± 0.80	0.89 ± 0.79
CL (Gomez et al, 2010)	4.313 ± 3.72	0.52 ± 0.41	0.51 ± 0.40
ROTM (Sha et al., 2016)	3.832 ± 2.63	0.70 ± 0.66	0.73 ± 0.61
CM (Liu et al., 2011)	2.919 ± 2.07	0.80 ± 0.73	0.79 ± 0.61
Multiscale CBGC	**2.342 ± 1.42**	**0.94 ± 0.82**	**0.92 ± 0.82**
Multiscale CL	3.511 ± 2.32	0.75 ± 0.69	0.79 ± 0.66
Multiscale ROTM	4.009 ± 3.14	0.65 ± 0.54	0.69 ± 0.54
Multiscale CM	**2.452 ± 1.59**	**0.93 ± 0.84**	**0.90 ± 0.80**
Proposed method	**2.042 ± 1.09**	**0.96 ± 0.85**	**0.98 ± 0.88**

Table 11

Qualitative evaluations for benign BUSs (**Mean** ± **Standard Deviation**)

Algorithm	Accuracy (%)	Specificity (%)	Precision (%)	Sensitivity(%)
CBGC (Chiang et., 2010)	89.415 ± 10.12	81.235 ± 8.09	87.210 ± 10.46	93.405 ± 6.39
ACWE (Chan &Vese, 2001)	91.219 ± 9.10	85.216 ± 9.30	89.785 ± 9.61	94.213 ± 6.01
CL (Gomez et al, 2010)	78.717 ± 15.12	70.569 ± 9.09	80.520 ± 12.60	87.804 ± 10.73
ROTM (Sha et al., 2016)	82.432 ± 12.63	77.442 ± 9.46	84.590 ± 11.72	89.002 ± 9.01
CM (Liu et al., 2011)	87.761 ± 11.07	80.067 ± 8.03	86.544 ± 10.91	89.334 ± 8.45
Multiscale CBGC	**93.882 ± 7.62**	**86.512 ± 9.672**	**92.102 ± 9.66**	**95.721 ± 5.57**
Multiscale CL	91.411 ± 8.72	87.644 ± 9.756	89.872 ± 9.92	93.600 ± 6.74
Multiscale ROTM	90.659 ± 9.14	85.734 ± 9.408	88.431 ± 10.01	91.407 ± 7.79
Multiscale CM	**93.415 ± 7.89**	**86.435 ± 8.012**	**92.004 ± 9.88**	**95.321 ± 5.97**
Proposed method	**97.318 ± 5.27**	**90.442 ± 7.112**	**95.407 ± 4.08**	**97.312 ± 4.34**

Table 12
Qualitative evaluations for malignant BUSs (**Mean** ± **Standard Deviation**)

Algorithm	Accuracy (%)	Specificity (%)	Precision (%)	Sensitivity (%)
CBGC (Chiang et., 2010)	86.119 ± 13.87	75.292 ± 10.41	84.367 ± 13.47	89.206 ± 10.11
ACWE (Chan &Vese, 2001)	88.435 ± 12.70	79.241 ± 10.99	86.502 ± 12.98	90.313 ± 9.27
CL (Gomez et al, 2010)	73.231 ± 19.90	70.244 ± 12.09	71.205 ± 16.09	74.219 ± 16.23
ROTM (Sha et al., 2016)	84.451 ± 15.23	76.345 ± 12.46	81.010 ± 14.96	85.414 ± 13.22

CM (Liu et al., 2011)	85.092 ± 14.03	75.005 ± 12.08	82.932 ± 14.37	87.069 ± 12.91
Multiscale CBGC	**90.448 ± 11.22**	**84.006 ± 13.02**	**88.419 ± 11.25**	**92.316 ± 8.07**
Multiscale CL	89.340 ± 12.20	75.003 ± 11.03	87.784 ± 12.10	91.268 ± 8.94
Multiscale ROTM	87.090 ± 13.76	72.207 ± 10.03	85.311 ± 12.20	89.222 ± 10.18
Multiscale CM	**90.234 ± 11.78**	**84.450 ± 10.12**	**88.129 ± 11.82**	**92.798 ± 8.40**
Proposed method	**94.217 ± 9.38**	**87.060 ± 9.06**	**93.223 ± 9.29**	**96.653 ± 5.17**

Table 13
Qualitative evaluations for Cyst BUSs (**Mean** ± **Standard Deviation**)

Algorithm	Accuracy (%)	Specificity (%)	Precision (%)	Sensitivity (%)
CBGC (Chiang et., 2010)	88.631 ± 11.48	78.413 ± 9.05	86.102 ± 13.20	90.702 ± 7.49
ACWE (Chan &Vese, 2001)	90.005 ± 10.30	82.002 ± 9.43	88.212 ± 11.24	92.490 ± 6.54
CL (Gomez et al, 2010)	82.392 ± 15.99	72.390 ± 11.23	80.702 ± 17.21	84.670 ± 10.37
ROTM (Sha et al., 2016)	84.06 ± 13.48	71.742 ± 10.77	82.321 ± 14.42	86.098 ± 9.58
CM (Liu et al., 2011)	86.319 ± 12.30	75.632 ± 10.44	84.213 ± 13.23	88.789 ± 8.65
Multiscale CBGC	**92.703 ± 9.44**	**82.001 ± 9.74**	**92.102 ± 9.66**	**94.341 ± 5.32**
Multiscale CL	90.234 ± 10.07	80.40 ± 9.66	88.765 ± 10.69	92.255 ± 6.25
Multiscale ROTM	88.880 ± 11.09	78.551 ± 9.98	86.578 ± 13.12	90.609 ± 7.46
Multiscale CM	**92.992 ± 9.89**	**82.620 ± 9.77**	**90.235 ± 9.95**	**94.526 ± 5.89**
Proposed method	**96.457 ± 6.90**	**86.402± 9.82**	**94.509 ± 7.21**	**98.844 ± 3.34**

Table 14
Qualitative evaluations for fibroadenoma BUSs (**Mean** ± **Standard Deviation**)

Algorithm	Accuracy (%)	Specificity (%)	Precision (%)	Sensitivity (%)
CBGC (Chiang et., 2010)	92.205 ± 12.51	82.623 ± 10.49	90.541 ± 12.65	94.329 ± 9.47
ACWE (Chan &Vese, 2001)	93.451 ± 11.65	83.719 ± 10.03	91.504 ± 11.82	95.713 ± 8.82
CL (Gomez et al, 2010)	86.373 ± 17.23	76.443 ± 13.19	84.500 ± 16.76	88.580 ± 14.31
ROTM (Sha et al., 2016)	88.214 ± 14.77	76.792 ± 13.66	86.506 ± 14.74	90.321 ± 12.61
CM (Liu et al., 2011)	90.251 ± 13.74	79.070 ± 13.33	89.607 ± 13.31	92.632 ± 10.45
Multiscale CBGC	**94.284 ± 11.42**	**84.449 ± 11.62**	**92.223 ± 10.60**	**96.221 ± 7.22**
Multiscale CL	90.113 ± 13.72	80.780 ± 12.79	88.342 ± 13.92	92.430 ± 10.04
Multiscale ROTM	89.626 ± 15.01	79.200 ± 13.43	87.242 ± 14.14	91.326 ± 10.79
Multiscale CM	**94.038 ± 11.98**	**84.004 ± 11.08**	**92.400 ± 10.98**	**96.021 ± 7.97**
Proposed method	**96.753 ± 4.74**	**86.213 ± 12.39**	**94.450 ± 3.78**	**98.216 ± 4.01**

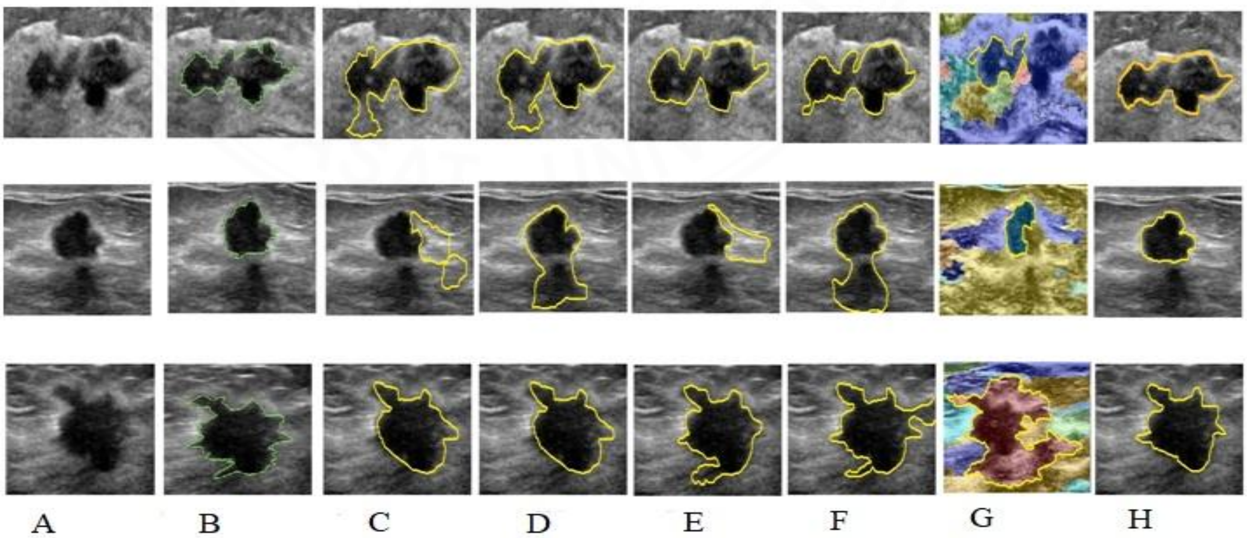

Fig. 22. The proposed and the reference multi-scale methods. (A) Original image, (B) Ground truth, (C) CBGC, (D) ACWE, (E) CL, (F) ROTM, (G) CM, and (H) Proposed method.

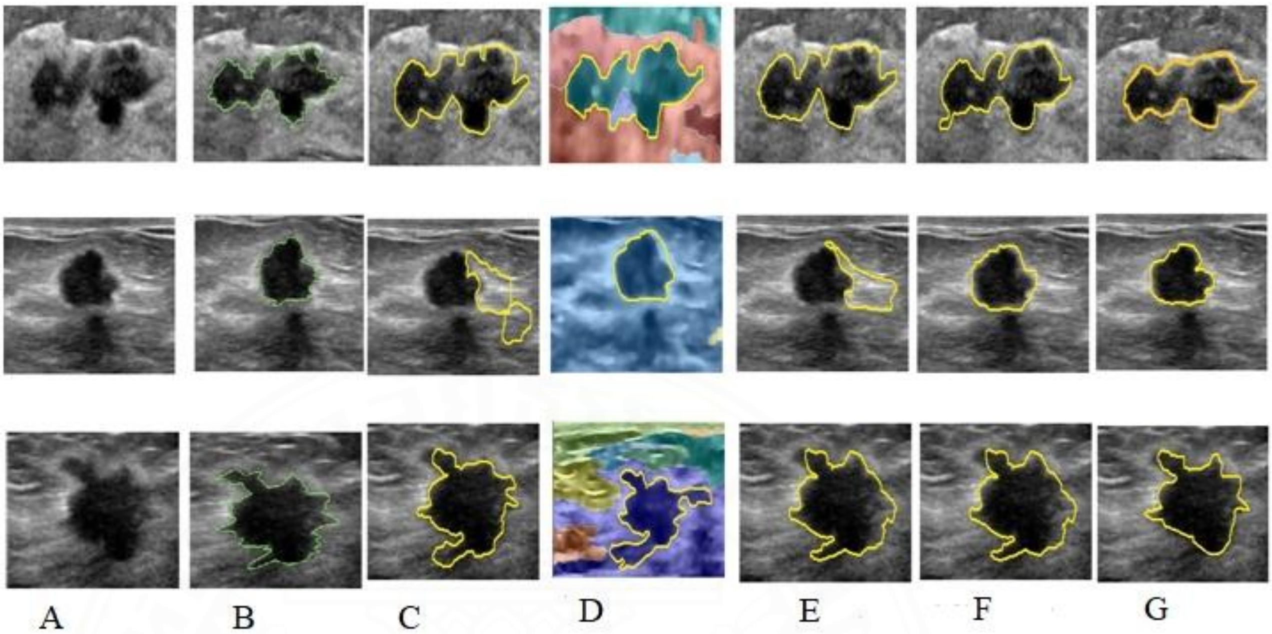

Fig. 23. The proposed and the reference multi-scale methods. (A) Original image, (B) Ground truth, (C) Multi-CBGC, (D) Multi-CL, (E) Multi-ROTM, (F) Multi-CM, and(G) Proposed method.

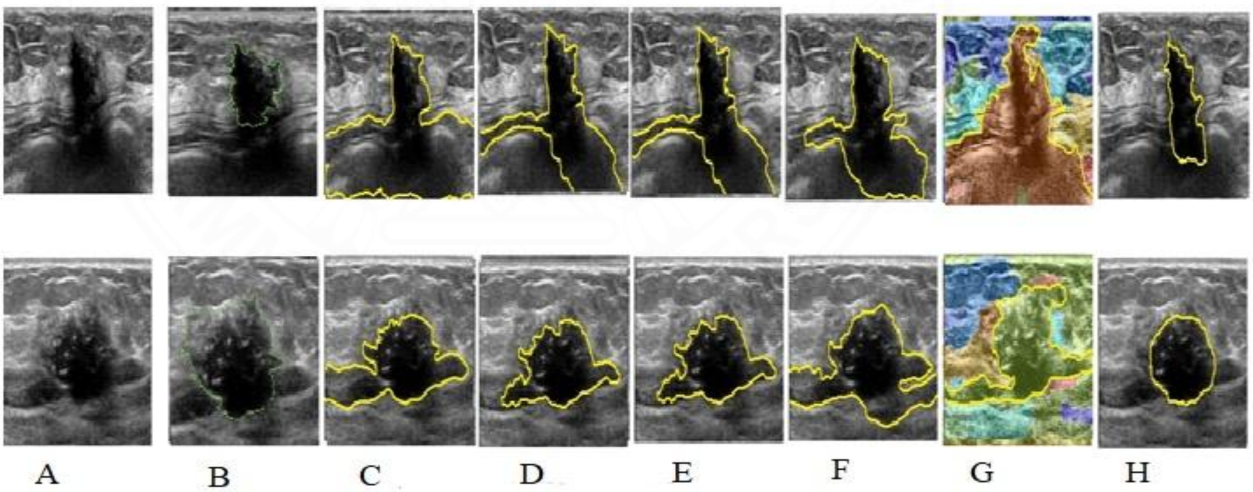

Fig. 24. Failed segmentation. (A) Original image, (B) Ground truth, (C) CBGC, (D) ACWE, (E) CL, (F) ROTM, (G) CM, and (H) Proposed method.

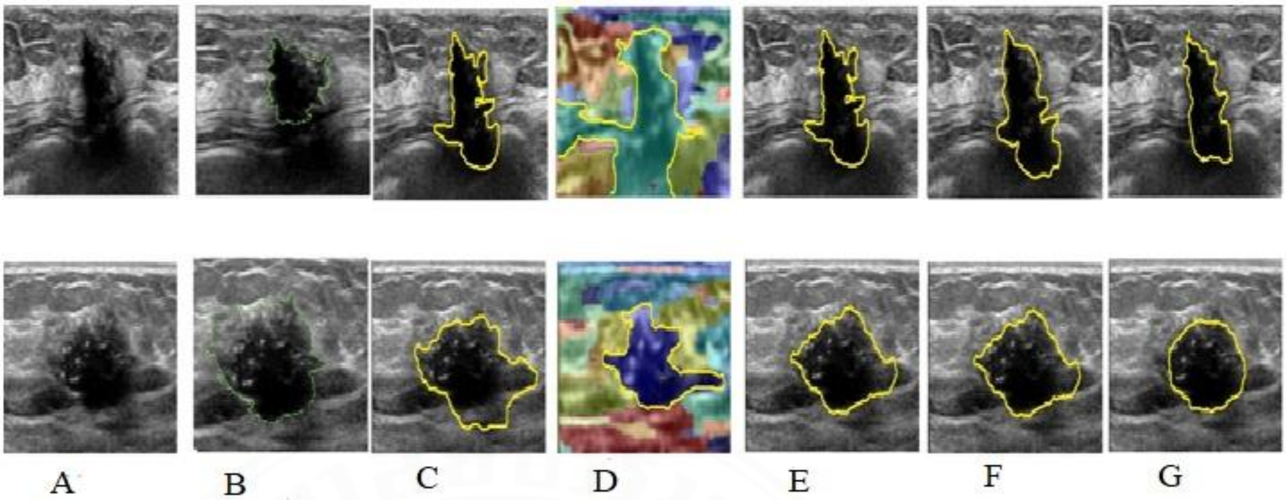

Fig. 25. Failed segmentation. (A) Original image, (B) Ground truth, (C) Multi-CBGC, (D) Multi-CL, (E) Multi-ROTM, (F) Multi-CM, and(G) Proposed method.

The above indicates that the proposed method is effective for the segmentation of breast ultrasounds. Visual comparison between the proposed method and the state-of-the-art methods is presented in figs 22 and 23. In all cases, the proposed approach outperforms the competitors. The qualitative results of cases 1, 2, 3, and 4 are given in tables 10 to 14, respectively. Experiments indicate that CL produces the worst performance for benign, malignant, fibroadenoma, and cyst BUS images. CBGC, ACWE, ROTM, and CM produce relatively good results however, their performance is not satisfactory. ACWE produces the best result if the multiscale is not applied (see fig. 26).

Multiscale methods produce better results than methods without multiscale. For example, the segmentation of benign images, CBGC, ACWE, CL, ROTM, CM, multiscale CBGC, multiscale CL, multiscale ROTM, and multiscale CM produced accuracies of 89%, 91%, 78%, 82%, 87%,93%,91%,90%, and 93%, respectively, whereas the proposed method produced an accuracy of 97%. For the malignant, fibroadenoma, and cyst BUS images the proposed method also outperformed the competing methods. The multiscale CBGC and CM produce the best results when compared with other methods (apart from the proposed method).

However, the proposed method produces the best accuracy (see figs 26, 27). Although the test methods performed well, they fail on images with a large number of shadows and a high level of speckle noise. The relevant examples are depicted in Figs. 24 and 25.

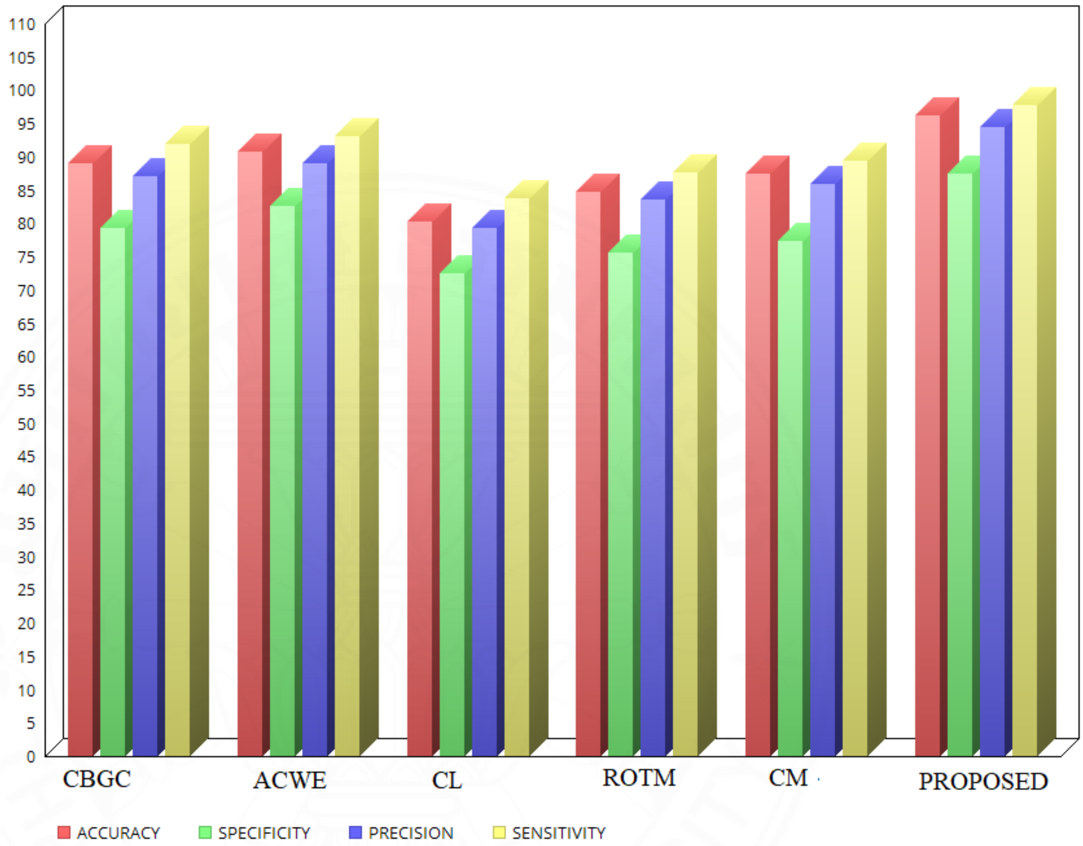

Fig. 26. The proposed method vs. the reference methods without multiscale

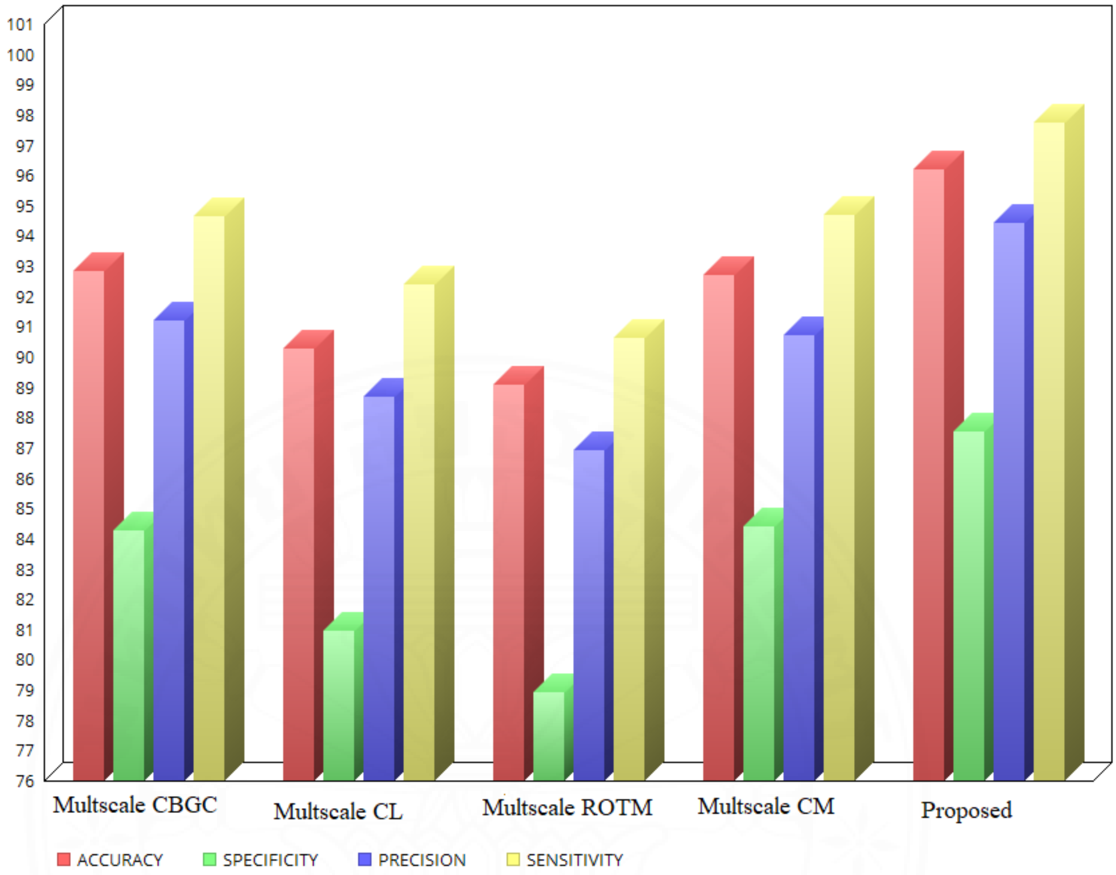

Fig. 27. The proposed method vs. the reference methods with multiscale

5.3 BUS images degraded by Gaussian noise

In every experiment, it is important to test for robustness; therefore, the robustness of the proposed method under various Gaussian noise levels is tested. Gaussian noise is a statistical noise with a probability density function equal to normal noise. The robustness of the proposed method is tested with the Gaussian noise levels of 0.005, 0.007, 0.009, and 0.01 (see Fig. 28, Tables 15).

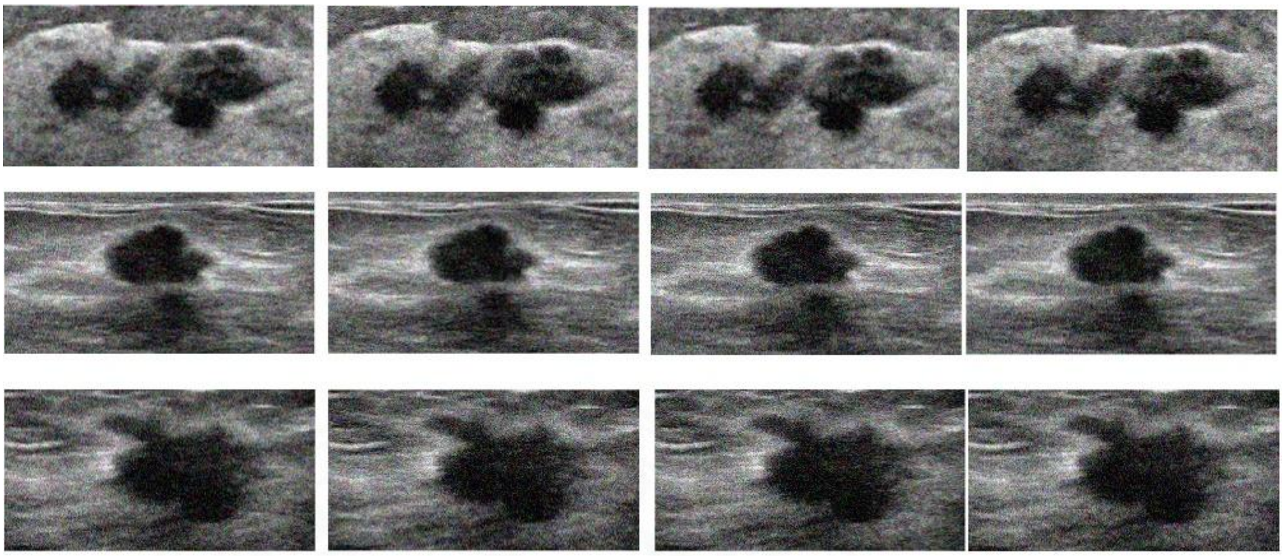

(a) 0.005 noise level (b) 0.007 noise level (c) 0.009 noise level (d) 0.01 noise level

Fig.28. BUS images subjected to different noise levels.

Table 15

Overall results for the quantitative evaluations and shape similarity for the different levels of Gaussian noise.

Gaussian Noise Level	Algorithm	Hausdorff Distance	JSC	DSC
0.005	Multiscale CBGC	3.602 ± 2.77	0.82 ± 0.74	0.81 ± 0.70
	Multiscale CL	**3.010 ± 2.52**	**0.85 ± 0.79**	**0.84 ± 0.77**
	Multiscale ROTM	4.790 ± 3.56	0.60 ± 0.52	0.63 ± 0.50
	Multiscale CM	**3.471 ± 2.85**	**0.85 ± 0.79**	**0.84 ± 0.72**
	Proposed method	**2.642 ± 1.57**	**0.92 ± 0.80**	**0.93 ± 0.81**
0.007	Multiscale CBGC	3.911 ± 2.88	0.79 ± 0.64	0.79 ± 0.64
	Multiscale CL	**3.421 ± 2.78**	**0.82 ± 0.70**	**0.80 ± 0.70**
	Multiscale ROTM	4.999 ± 3.79	0.52 ± 0.50	0.53 ± 0.49
	Multiscale CM	**3.73 ± 2.99**	**0.80 ± 0.74**	**0.79 ± 0.67**
	Proposed method	**2.702 ± 1.70**	**0.90 ± 0.81**	**0.91 ± 0.82**

0.009	Multiscale CBGC	3.822 ± 2.81	0.80 ± 0.69	0.80 ± 0.70
	Multiscale CL	**3.201 ± 2.62**	**0.83 ± 0.73**	**0.83 ± 0.73**
	Multiscale ROTM	4.884 ± 3.62	0.57 ± 0.51	0.57 ± 0.51
	Multiscale CM	**3.581 ± 2.89**	**0.82 ± 0.76**	**0.82 ± 0.76**
	Proposed method	**2.976 ± 1.87**	**0.90 ± 0.79**	**0.90 ± 0.79**
0.01	Multiscale CBGC	3.902 ± 2.97	0.84 ± 0.73	0.84 ± 0.73
	Multiscale CL	**3.111 ± 2.60**	**0.86 ± 0.79**	**0.85 ± 0.78**
	Multiscale ROTM	4.777 ± 3.52	0.70 ± 0.62	0.73 ± 0.64
	Multiscale CM	**3.500 ± 2.75**	**0.84 ± 0.79**	**0.84 ± 0.79**
	Proposed method	**2.603 ± 1.63**	**0.93 ± 0.81**	**0.93 ± 0.81**

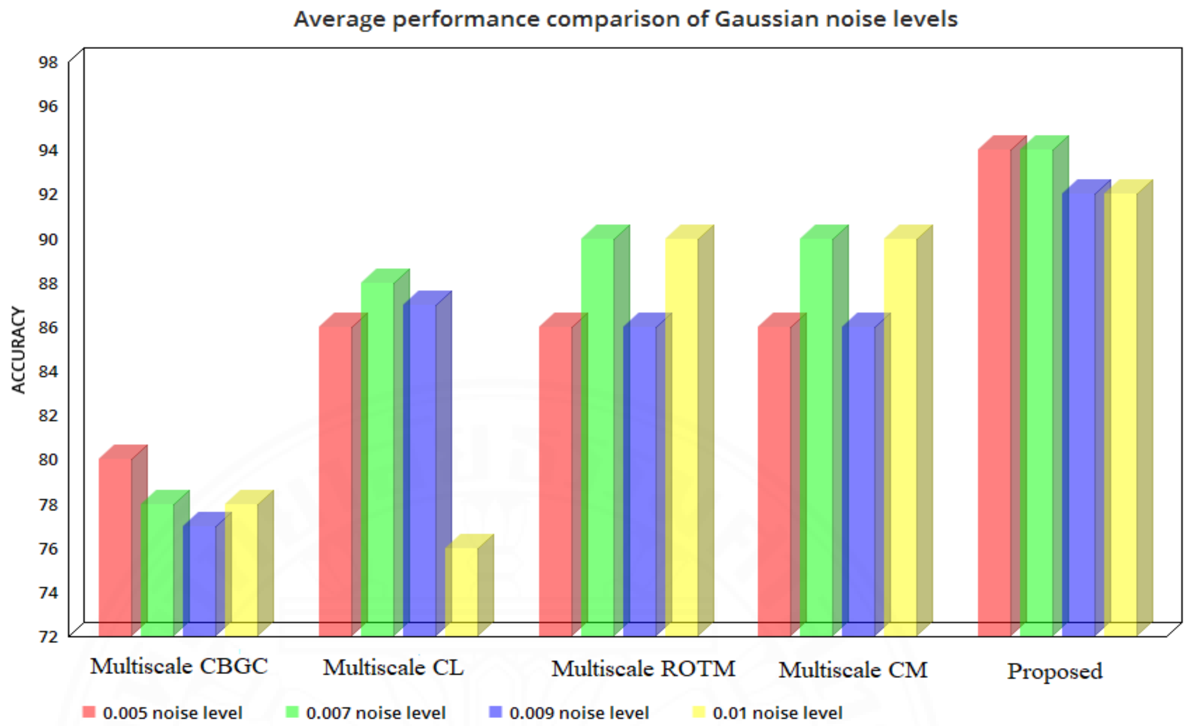

Fig. 29. The proposed method vs. the reference methods for different levels of Gaussian noise.

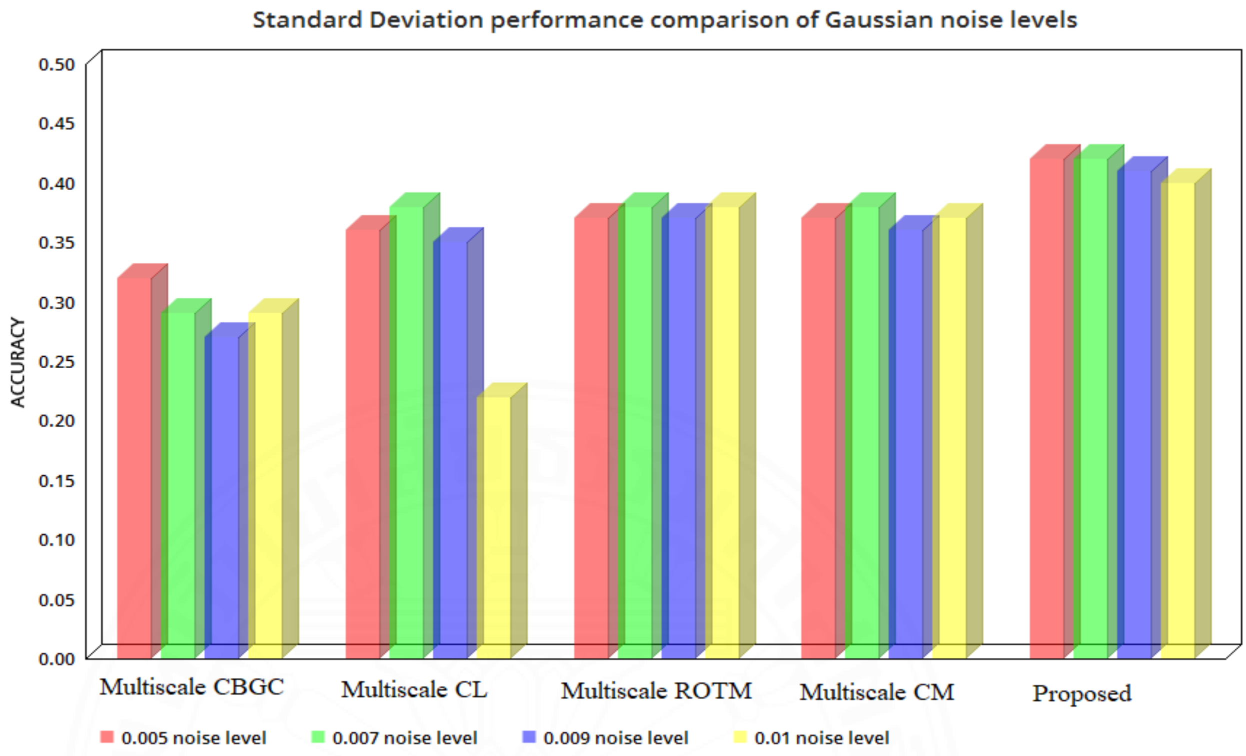

Fig. 30. Standard deviation by the proposed method vs. the reference methods for different levels of Gaussian noise.

Despite the addition of Gaussian noise, the proposed method still outperforms other methods. Although quantitative results are lower for images degraded with Gaussian noise, they are satisfactory and indicate that multiscale methods can withstand noise of different levels. Figs. 29 and 30 depict overall statistical analysis of levels of images degraded by noise.

CHAPTER 6
CONCLUSION AND FUTURE RESEARCH

6.1 Conclusion

The proposed novel combination of the speckle reduction filters outperforms 11 conventional and state-of-the-art methods, as applied to synthetic and BUS images. The performance of the method is measured using a combination of segmentation algorithms and segmentation criteria. The attained advantages in segmentation and experiments on synthetic images show that the MSHM outperforms these algorithms on BUS images, in terms of the standard reference-image based measures.

To segment the images, a novel multiscale superpixel method for the segmentation of BUS images based on the boundary efficient graph cut method is presented. A real dataset of breast ultrasounds obtained from Thammasat University Hospital is used for the evaluation. Specifically, a multiscale image from the original BUS image is created. Subsequently, the distance transforms superpixel decomposition of the multiscale images are generated before performing final segmentation. A novel segmentation that combines shape symmetry analysis with the graph cut method is adapted. The validation experiments proved that the proposed method outperformed the state-of-the-art segmentation methods with an average segmentation accuracy of 94%. In addition, the method is simple to understand and easy to replicate. Finally, several procedures to improve the medical applicability by balancing the accuracy and computational costs are performed. An enhanced superpixel method that does not involve additional memory consumption is introduced. The proposed method does not exclude the screening procedure during clinical examinations. However, it complements the clinical examinations and serves as the second opinion.

6.2 Limitation

It should be noted that the proposed method has several advantages over other methods, including (1) effective noise removal of both speckle and Gaussian noise, (2) effective segmentation of breast ultrasounds despite their inherent low quality, and

(3) the easy use for diagnosis by clinicians. However, the proposed method is limited by specific training. The methods are tested with data acquired from Philips iU22 ultrasound and LOGIQ E9 ultrasound machines. Although several high-quality studies have been conducted with our database, majority of the existing database does not include the ground truth.

6.3 Future Research

Analysis of the method using a variety of databases is a subject of future research. In future research, we recommend that this approach be used in the study of other kinds of ultrasound images (kidneys or thyroids) to validate the performance and accuracy of the proposed model. In addition, our method may be incorporated with deep learning networks to produce a robust algorithm.

APPENDIX

Main function

1. *Define the specific dataset*
2. *Open BUS image dataset.*
3. *Initialize the images in the dataset*
4. *while it is not the end of file:*
5. *read the next line from file*
6. *if :it failed to read the next line, stop the loop.*
7. *else: call the subfunction 1 that perform pre-processing*
8. *using subfunction 1 determine the pre-process images,*
9. *if: subfunction 1 completes, start subfunction 2*
10. *else: stop the loop*
11. *using subfunction 2 determine the segmented images,*
12. *save segmented image in designated location*
13. *End.*

SubFunction 1

Input: Grayscale BUS Image I

1: I_m ← *Multiscale* (I)

2: Create multiscale of image (I)

3: I_{Wf} ← *WF* (I_m)

4: Perform initial filtering with the weiner filter on images (I_m)

5: I_{Fbf} ← *FBF* (I_{Wf})

6: Perform speckle reduction with the fast bilateral filter on images (I_{Wf})

7: I_{Wdaf} ← *WDAF* (I_{Fbf})

8: Remove artifact with wavelet decomposition anisotropic filter on images (I_{Fbf})

Output: preprocessed BUS image (I_{pre})

SubFunction 2

Input: Preprocessed Images I_{pre}

<u>*Distance transform/pixel seed measure*</u>

Step 1: Clustering and superpixel method

- *Cluster assignment pixel with nearest cluster centre*
- *Create and perform cluster inspection for all scales*
- *Update cluster centre*
- *Create the object alignment boundary*
- *Create homogeneous and compactness appearance*

<u>Boundary efficient graph cut/final fusion</u>

Step 2: Segment image

- *Create a shape symmetry on image of step 4*
- *Perform graph cut segmentation*

<u>Model evaluation</u>

Step 3: Model evaluation

- *Evaluate the performance on the ultrasound in the dataset*
- *Add various type of noise*
- *Assess the performance of the proposed technique utilizing ground truth*

Output: Final segmentation (I_{mas}*)*

Link to code:
https://www.dropbox.com/s/qto1kdq6hiy9pko/dissertation_code.txt?dl=0

REFERENCES

Achanta, R., Shaji, A., Lucchi, K., Fua,A., &Susstrunk, P. (2012). SLIC superpixels compared to state-of-the-art superpixel methods. *IEEE Transactions on Pattern Analysis and Machine Intelligence*, 34, 2274–2281.

Adabi, S., Rashedi, E., Clayton, A., Mohebbi-Kalkhoran, H., Chen, X. W., Conforto, S., & Nasiriavanaki, M. (2018). Learnable despeckling framework for optical coherence tomography images, *Journal of Biomedical Optics*, 23(1), 1–12.

Adam,D., Beilin-Nissan,S., Friedman,Z.,&Behar, V. (2006). The combined effect of spatial compounding and nonlinear filtering on the speckle reduction in ultrasound images, *Ultrasonics*, 44 (2), 166–181.

Ahmed, L.J. (2018). Discrete shearlet transform based speckle noise removal in ultrasound images. *National Academy Science Letters* 41, 91-95.

Arias-Castro, E., &Donoho, D. L. (2009). Does median filtering truly preserve edges better than linear filtering?, *Annals of Statistics*, 37 (3), 1172–2009.

Al-Dhabyani, W., Gomaa, M., Khaled, H.,& Fahmy, A. (2020). Dataset of breast ultrasound images, *Data in Brief*, 28, 1048.

Altarawneh, N. M., Luo, S., Regan, B., Sun, C., & Jia, F. (2014). Global threshold and region-based active contour model for accurate image segmentation. Signal & Image Processing, 5(3), 1

Anita, G., Jyoti, G., Sandeep, M., Kavita, C., &Deepika, (2011). De-speckling of Medical Ultrasound Images using Wiener Filter and Wavelet Transform, 2(3), 2230 -7109.

Anscombe, F.J. (1948). The transformation of Poisson, binomial and negative binomial data,
Biometrika, 246-254

Avanaki, M.R.N., Cernat, R., Tadrous, P. J., Tatla, T., Podoleanu, A. G., & Hojjatoleslami, S A. (2013). Spatial compounding algorithm for speckle reduction of dynamic focus oct images, *Photonics Technology Letters IEEE*, 25(15), 1439-1442.

Azzari, L., Foi, A. (2016). Variance stabilization for noisy+estimate combination in iterative Poisson denoising, *IEEE Signal Processing Letters*, 23 (8), 1086-1090

Bag, S., Kumar, S.,&Tiwari, M. (2019). An efficient recommendation generation using relevant Jaccard similarity, *Information Sciences*, 483, 53–64.

Bajaj, K., Singh, D. K.,&Ansari, M. A. (2019). Autoencoders Based Deep Learner for Image Denoising, *Procedia Computer Science*, 171, 1535–1541.

Baselice, F., Ferraioli, G., Ambrosanio, M., Pascazio, V.,& Schirinzi, G. (2018). Enhanced Wiener filter for ultrasound image restoration, *Computer Methods and Programs in Biomedicine*,153, 71–81.

Beucher, S & Meyer, F. (1993). The morphological approach to segmentation: the watershed transformation, in: Mathematical Morphology in Image Processing, Marcel Dekker Inc., New York, 433–481.

Byra, M., Jarosik, P., Szubert,A., Galperin, M., Ojeda-Fournier,H., Olson,L., O'Boyle, M., Comstock,C.,&Andre,M. (2020). Breast mass segmentation in ultrasound with selective kernel U-Net convolutional neural network, *Biomedical Signal Processing and Control*, 61, 102027.

Can-Fei, L., Yao-Nan, W., Chang-Yan,X.,&Xia,L., (2012). A new speckle reducing anisotropic diffusion for ultrasonic speckle, *Acta Automat. Sin.* 38, 412–418.

Chan, T.F., &Vese, L.A., (2001). Active contours without edges, IEEE Trans. Image Process. 10, 266–277.

Chen, L.-C., Papandreou, G., Schroff,F., &Adam H.(2017). Rethinking atrous convolution for semantic image segmentation. arXiv preprint arXiv:1706.05587

Chen, T.,& Metaxas, D. (1998). Image segmentation based on the integration of Markov random fields and deformable models, *MICAAI*,

Chiang, H.-H., Cheng, J.-Z., Hung, P.-K.,Liu, C.-Y., Chung, C.-H.,&Chen,C.-M.(2010). Cell-based graph cut for segmentation of 2D/3D sonographic breast images, in: Proceedings of the IEEE ISBI, 177–180.

Cousty, J., Bertrand, G., Najman,L.,&Couprie, M. (2009). Watershed cuts: minimum spanning forests and the drop of water principle, *IEEE Trans. Pattern Anal. Mach. Intell*. 31, 1362–1374.

Damodaran,N., Ramamurthy,S., Velusamy, S.,&Manickam, G.K.(2012). Speckle noise reduction in ultrasound biomedical-scan images using discrete topological derivative, *Ultrasound Med. Biol*. 38(2), 276–286.

Daoud,M.I.,Baba,M.M.,Awwad,F., Al-Najjar,M.,&Tarawneh, E.S. (2012). Accurate segmentation of breast tumors in ultrasound images using a custom-made active contour model and signal-to-noise ratio variations, in*: Proceedings of the IEEE SITIS*, 137–141.

Daoud, M.I., Atallah, A. A., Awwad, F., Al-Najjar, M.,&Alazrai, R. (2019). Automatic superpixel-based segmentation method for breast ultrasound images, *Expert Systems with Applications*, 121, 78–96.

De Fontes, FPX., Barroso, G.A., Coupé, P., &Hellier, P. (2011). Real time ultrasound image denoising , *Journal of Real-Time Image Processing*, 6(1):15–22.

Digabel, H.,&Lantu´ejoul, C. (1978). *Iterative algorithms, in Proc. 2nd European Symp. Quantitative Analysis of Microstructures in Material Science, Biology and Medicine*, 85–89.

Dirami, A., Hammouche, K., Diaf, M., & Siarry, P. (2013). Fast multilevel thresholding for image segmentation through a multiphase level set method. Signal Processing, 93(1), 139-153.

Donoho, D.L., & Johnstone, I.M. (1994). Ideal spatial adaptation by wavelet shrinkage, *Biometrika*, 81, 425–455.

Dore, V., Moghaddam, R.F., & Cheriet, M. (2011). Non-Local Adaptive Structure Tensors. Application to Anisotropic Diffusion and Shock Filtering, *Image and Vision Computing*, 29, 730-743.

Drukker, K., Giger, M.L., Horsch, K., Kupinski, M.A., Vyborny, C.J.,&Mendelson, E.B. (2002). Computerized lesion detection on breast ultrasound, *Med Phys*, 29, 1438-1446

Eybposh, M. H.,Turani,Z., Mehregan, D., &Nasiriavanaki, M. (2018). Cluster-based filtering framework for speckle reduction in OCT images, *Biomedical Optics Express*, 9(12), 6359–6373.

Fan, H., Meng, F., Liu, Y., Kong, F., Ma, J.,&Lv, Z. (2019). A novel breast ultrasound image automated segmentation algorithm based on seeded region growing integrating gradual equipartition threshold, *Multimed Tools Appl* 78,27915–27932.

Fang, Y.,&Zeng, T. (2020). Learning deep edge prior for image denoising, *Computer Vision and Image Understanding*, 200, 103044.

Felzenszwalb, P.F.,&Huttenlocher, D.P. (2004). Efficient graph-based image segmentation, *International Journal of Computer Vision*, 59(2), 167–181.

Filipczuk, P., Kowal, M., & Obuchowicz, A. (2011). Fuzzy clustering and adaptive thresholding based segmentation method for breast cancer diagnosis. In Computer Recognition Systems 4 (pp. 613-622). Springer Berlin Heidelberg

Gai, S.,& Bao, Z. (2019). New image denoising algorithm via improved deep convolutional neural network with perceptive loss, *Expert Systems With Applications*, 138, 112815.

Gai, S., Zhang, B., Yang, C.,&Yu, L. (2018). Speckle noise reduction in medical ultrasound image using monogenic wavelet and Laplace mixture distribution, *Digit. Signal Process. A Rev. J.* 72, 192–207.

Gao, L., Liu, X., & Chen, W. (2012). Phase-and gvf-based level set segmentation of ultrasonic breast tumors, *Journal of Applied Mathematics*, 2012, 1–22.

Gao, Z., Bu, W., Zheng, Y.,&Wu, X. (2017). Automated layer segmentation of macular OCT images via graph-based SLIC superpixels and manifold ranking approach, *Computerized Medical Imaging and Graphics* 55, 42–53.

Garg, A.,&Khandelwal, V.(2018). Combination of spatial domain filters for speckle noise reduction in ultrasound medical images, *Adv. Electr. Electron. Eng*. 15 (5),857–865.

Ghosh, S., &Chaudhary, KN. (2016). On fast bilateral filtering using Fourier kernels. *IEEE Signal Process Letters*, 23(5), 570–593.

Gibbs, C. H. (1925). Phenomenon in Fourier's Integrals, *Nature* 116**,** 312–313. https://doi.org/10.1038/116312c0

G_omez-flores, W.,&Aruiz-ortega, B. (2016). New fully automated method for segmentation of breast lesions on ultrasound based on texture analysis, *Ultrasound in Medicine & Biology*, 42(7), 1637–1650.

Gomez, W., Leija, L., Alvarenga,A., Infantosi, A.,& Pereira, W. (2010). Computerized lesion segmentation of breast ultrasound based on marker-controlled watershed transformation, *Medical physics*, 37(1), 82–95.

Gu, P., Lee, W., Roubidoux, M. A., Yuan, J., Wang, X.,& Carson, P. L. (2016). Automated 3D ultrasound image segmentation to aid breast cancer image interpretation, *Ultrasonics*, 65, 51–58.

Guo, Y., S¸eng¨ur, A., &Tian, J.W. (2015). A Novel Breast Ultrasound Image Segmentation Algorithm Based on Neutrosophic Similarity Score and Level Set, *Computer Methods and Programs in Biomedicine*, 123, 43-53.

Han, L., Huang, Y., Dou, H., Wang,S.,Ahamad, S., Luo, H., Liu, Q., Fan, J.,&Zhang, J. (2020). Semi-supervised segmentation of lesion from breast ultrasound images with attentional generative adversarial network, *Computer Methods and Programs in Biomedicine* 189, 105275.

Harb, S.M.E., Isa, N.A.M.,&Salamah, S.A. (2015). Improved image magnification algorithm based on Otsu thresholding, *Computers and Electrical Engineering* 46, 338–355.

Hiramatsu, Y., Muramatsu, C., Kobayashi, H., Hara, T., &Fujita, H. (2017). Automated detection of masses on whole breast volume ultrasound scanner: false positive reduction using deep convolutional neural network. In: *Proceedings of the SPIE Medical Imaging*.

He, K., Sun, J.,&Tang, X.,(2010). Guided image filtering, in: Proceedings of 11th European Conference on Computer Vision, Berlin, 1–14.

Hong, I., Hwang, Y.,&Kim, D. (2019). Efficient deep learning of image denoising using patch complexity local divide and deep conquer, *Pattern Recognition*, 96, 106945.

Horsch, K., Giger, M.L., Venta, L.A., &Vyborny, C.J. (2001). Automatic segmentation of breast lesions on ultrasound. *Medical Physics* 28, 1652–1659.

Hosch, K., Giger, M.L., Venta, L., & Vyborny, C. J.,(2002). Computerized diagnosis of breast lesions on ultrasound, *Medical Physics* 29 (2), 157–164.

Hosmer, D.W.,&Lemeshow, S. (2000).Applied Logistic Regression, Wiley-Interscience

Huang, Y. L., & Chen, D. R. (2004). Watershed segmentation for breast tumor in 2-D sonography. Ultrasound in medicine & biology, 30(5), 625-632.

Huang, Q., Chen, Y.,Liu, L., Tao, D.,&Li, X. (2020). On combining biclustering mining and Adaboost for breast tumor classification, *IEEE Transactions on Knowledge and Data Engineering*, 32(4), 728-738.

Huang,Q., Huang, X., Liu,L., Lin,Y., Long, X.,& Li, X. (2018). A case-oriented web-based training system for breast cancer diagnosis, *Computer Methods and Programs in Biomedicine***,** 156, 73–83.

Huang, Q., Huang, Y., Luo, Y., Yuan, F.,& Li, X. (2020). Segmentation of breast ultrasound image with semantic classification of superpixels, *Medical Image Analysis* 61, 101657.

Huang, Q., Lee, S., Liu, L., Lu, M., Jin, L.,&Li, A. (2012) A robust graph-based segmentation method for breast tumors in ultrasound images, *Ultrasonics*, 52 (2012) 266–275.

Huang, Q., Bai, X., Li, Y., Jin, L.,&Li, X. (2014). Optimized graph-based segmentation for ultrasound images, *Neurocomputing*, 129, 216–224.

Huang, Q., Yang,F., Liu, L.,& Li, X. (2015). Automatic segmentation of breast lesions for interaction in ultrasonic computer-aided diagnosis, *Information Sciences*, 314, 293–310.

Huang Y.L., &Chen D.R. (2004). Watershed segmentation for breast tumor in 2-D sonography

Ultrasound Med. Biol., 30, 625-632.

Ikedo, Y., Fukuoka, D., Hara, T., Fujita, H., Takada, E., Endo, T.,&Morita, T. (2007). Development of a fully automatic scheme for detection of masses in whole breast ultrasound images, *Med. Phys*., 34, 4378-4388

Ilesanmi, A.E., Idowu, O.P., & Makhanov, S.S. (2020). Multiscale superpixel method for segmentation of breast ultrasound, *Computers in Biology and Medicine*, 125, 103879.

Jain, L., & Singh, P. (2020). A novel wavelet thresholding rule for speckle reduction from ultrasound images, Journal of King Saud University - Computer and Information Sciences, Jaroša, M., Strakoša,P.,Karásek, T.,Ríha,L.,Vašatová, A.,Jarošová, M.,&Kozubek,T. (2017). Implementation of K-means segmentation algorithm on Intel Xeon Phi and GPU: Application in medical imaging, *Advances in Engineering Software*, 103, 21–28.

Jiang, P., Peng, J., Zhang, G., Cheng, E., Megalooikonomou, V.,&Ling, H. (2012). Learning-based automatic breast tumor detection and segmentation in ultrasound images, in: *Proceedings of the IEEE ISBI*, 1587–1590.

Jin, B., You, S.J.,&Cho, N.I. (2015). Bilateral image denoising in the Laplacian subbands, *Journal of Image Video Processing*, 26, 2–12.

Karunanayake, N., Aimmanee, P., Lohitvisate, W.,& Makhanov, S.S. (2020). Particle method for segmentation of breast tumors in ultrasound images, *Mathematics and Computers in Simulation*, 170, 257‒284.

Keatmanee, C., Chaumrattanakul, U., Kotani, K.,&Makhanov, S. S. (2019). Initialization of Active Contours for Segmentation of Breast Cancer via Fusion of Ultrasound, Doppler, and Elasticity Images, *Ultrasonics*, 94, 438-453.

Kim, J.J., Nam, J., &Jang, I.G. (2018). Fully automated segmentation of a hip joint using the patient-specific optimal thresholding and watershed algorithm, *Computer Methods and Programs in Biomedicine*, 154, 161–171.

Kim, Y.T. (1997). Contrast enhancement using brightness preserving bi-histogram equalization, *IEEE Trans. Consum. Electron*., 43, 1-8.

Kiryati, N., Gofman, Y. (1998). Detecting Symmetry in Grey Level Images: The Global Optimization Approach. *International Journal of Computer Vision*, 29, 29–45 https://doi.org/10.1023/A:1008034529558

Kriti, J., Virmani, R.,&Agarwal, (2019). Effect of despeckle filtering on classification of breast tumors using ultrasound images, *biocybernetics and biomedical engineering*, 39, 536 – 560.

Kruskal, J.B. (1956). On the shortest spanning subtree of a graph and the traveling salesman problem, *Proc. Am. Math. Soc*., 7 (1), 48-50

Kumar, V., Webb, J.M., Gregory, A., Denis, M., Meixner, D.D., Bayat, M., Whaley, D.H., Fatemi, M.,&Alizad, A. (2018). Automated and real-time segmentation of suspicious breast masses using convolutional neural network. *PLoS ONE* 13, e0195816.

Kwak, J.I., Kim, S.H., &Kim, N.C. (2005). RD-based seeded region growing for extraction of breast tumor in an ultrasound volume, *Proceedings of the Computational Intelligence and Security, Springer*, 799-808

Lai, Y., Huang, Y., Wang, D., Tiu, C., Chou, Y., &Chang, R. (2013). Computer-aided diagnosis for 3-d power doppler breast ultrasound, *Ultrasound in Medicine and Biology*, 39(4), 555–567.

Lang, I., Levy, M. S.,&Spitzer, H. (2016). Multi-scale texture-based level-set segmentation of breast B-mode images, *Computers in Biology and Medicine*, 72, 30 - 42.

Lee, S., Huang, Q., Jin, L., Lu, M.,&Wang, T. (2010). A Graph-Based, Segmentation method for breast tumors in ultrasound images, in: *Proceedings of IEEE iCBBE*, 1–4.

Lee, S., Negishi, M., Urakubo, H., Kasai, H.,&Ishii, S. (2020). Mu-net: Multi-scale U-net for two-photon microscopy image denoising and restoration, *Neural Networks*, 125, 92–103.

Li, Y., Sun, J., Tang, C.K.,&Shum, H.Y. (2004). Lazy snapping, *ACM Transaction Graph*, 303-308

Liu, Y., Chen, Y., Han, B., Zhang, Y., Zhang, X.,&Su, Y. (2018). Fully automatic Breast ultrasound image segmentation based on fuzzy cellular automata framework, *Biomedical Signal Processing and Control*, 40, 433–442.

Liu, J.,Chen, J., Liu,X., Chun,L., Tang,J., &Deng,Y., (2011). Mass segmentation using a combined method for cancer detection, *BMC Syst Biol*., 5(3): 6.

Lo, C.M.,Chen,R.T.,Chang,Y.C., Yang,Y.W., Hung, M.J.,Huang,C.S.,&Chang,R.F. (2014). Multi-dimensional tumor detection in automated whole breast ultrasound using topographic watershed, *IEEE Trans. Med. Imaging*, 33, 1503–1511.

Lyu, Z., Zhang, C.,&Han, M. (2020). A nonsubsampled countourlet transform based CNN for real image denoising, *Signal Processing: Image Communication*82, 115727.

Machairas, V., Faessel, M., Crdenas-Pea, D., Chabardes,T.,& Walter, T. (2015). Decencire, Waterpixels. *IEEE Transactions on Image Processing*, 24 (11), 3707−3716.

Madabhushi, A.,& Metaxas, D. (2002). Automatic boundary extraction of ultrasonic breast lesions, Proceedings of the IEEE ISBI (2002), pp. 601-604

Mandelbrot, BB. (1982). The fractal geometry of nature. Rev. ed. New York (NY): W.H. Freeman and Company; 468

Maolood, I. Y., Yea, A.,&Lu, S. (2018). Thresholding for medical image segmentation for cancer using fuzzy entropy with level set algorithm. *Open Med-Warsaw*, 13, 374–383.

Massich, J., Meriaudeau, F., Pérez, E., Martí, R., Oliver, A., & Martí, J. (2010). Lesion Segmentation in Breast Sonography. In: Martí, J., Oliver, A., Freixenet, J., Martí, R. (eds.) *IWDM LNCS Springer, Heidelberg*, 6136, 39–45.

Mateo, J.L.,& Fernndez-Caballero, A. (2009). Finding out general tendencies in speckle noise reduction in ultrasound images, *Expert System with Applications*, 36 (4), 7786–7797.

Meiburger, K. M., Acharya, U.R.,&Molinari,F. (2018). Automated localization and segmentation techniques for B-mode ultrasound images: A review, *Computers in Biology and Medicine* 92, 210–235.

Min, X.,Yingtao, Z., Cheng, H.D., Fei, X., Boyu, Z., &Jianrui D. (2018). Automatic breast ultrasound image segmentation: A survey. *Pattern Recognition*, *26*(8), 34-42.

Moon, W. K., Chang, S., Chang, J. M., Cho, N., Huang, C., Kuo, J.,& Chang, R. (2013). Classification of breast tumors using elastographic and b-mode features: comparison of automatic selection of representative slice and physician-selected slice of images, *Ultrasound in Medicine and Biology*, 39,(7), 1147–1157.

Mu, N., Xu, X., Zhang, X., & Lin, X. (2018). Discrete stationary wavelet transform based saliency information fusion from frequency and spatial domain in low contrast images, *Pattern Recognition Letters*, 115, 84–91.

Mustaqeem, A., Javed, A., & Fatima, T. (2012). An efficient brain tumor detection algorithm using watershed & thresholding based segmentation. International Journal of Image, Graphics and Signal Processing, 4(10), 34.

Nageswari, C.S., &Prabha, K.H. (2013). Despeckle process in ultrasound fetal image using hybrid spatial filters. *International Conference on Green Computing, Communication and Conservation of Energy*, 174–179.

Ng, V., Fung, B., &Lee, T. (2005). Determining the asymmetry of skin lesion with fuzzy borders, *Computers in Biology and Medicine*, 35 (2), 103–120.

Ning, G., Zhang, X.,& Liao, H. (2019). Morphological active contour without edge-based model for real-time and non-rigid uterine fibroid tracking in HIFU treatment, *Healthcare Technology Letters*, 6(12), 172–175.

Najman, L.,&Schmitt, M. (1996). Geodesic saliency of watershed contours and hierarchical segmentation, *IEEE Trans Pattern Anal Machine Intell*, 18 (12), 1163-1173

Omasi, C.,&Manduchi, R., (2006). Bilateral filtering for gray and color images, *Proc. 1998 IEEE Int. Conf. Computer Vision*, *Bombay, India electronics letters*, 42(7)

Osman, F. M., &Yap, M. H. (2020). Adjusted Quick Shift Phase Preserving Dynamic Range Compression method for breast lesions segmentation, Informatics in Medicine Unlocked 20, 100344.

Panigrahi, L., Verma, K., &Singh, B. K. (2019). Ultrasound image segmentation using a novel multi-scale Gaussian kernel fuzzy clustering and multi-scale vector field convolution, *Expert Systems With Applications* 115, 486–4 98.

Paris, S., &Durand, F., (2006). A fast approximation of the bilateral filter using a signal processing approach. *Int. J. Comput. Vis*., 81, 24-52

Parris, T., Wakefield, D., &Frimmer, H. (2013). Real world performance of screening breast ultrasound following enactment of Connecticut Bill 458, *Breast Journal*, 19 (1), 64–70.

Peng, Z., Qu, S.,& Li, Q. (2019). Interactive image segmentation using geodesic appearance overlap graph cut, *Signal Processing: Image Communication*, 78, 159–170.

Perona, P., &Malik, J. (1990). Scale-space and edge detection using anisotropic diffusion, *IEEE Trans Pattern Anal Mach Intell*, 12(7):629–639.

Pizer, S.M., Amburn, E.P., Austin, J.D., Cromartie, R., Geselowitz, A., Greer, T., ter Haar Romeny, B., Zimmerman, J.B.,&Zuiderveld, K. (1987). Adaptive histogram equalization and its variations, *Comput. Vis.Graph. Image Process.*, 39 (3), 355-368

Pons,G.,Martí, J., Martí, R.,Ganau,S., & Noble,J.A. (2016). Breast lesion segmentation combining B-mode and elastography ultrasound, *Ultrasonic Imaging*, 38(3), 209–224.

Pratt, W. K. (1972). Generalized Wiener Filtering Computation Techniques, *IEEE transactions on computers*, 21(7).

Qi, X., Zhang, L., Chen, Y., Pi, Y., Chen, Y., Lv, Q., &Yi, Z. (2019). Automated diagnosis of breast ultrasonography images using deep neural networks, *Medical. Image Analysis*. 52, 185–198.

Ramadan, H., Lachqar, C.,&Tairi, H. (2020). Saliency-guided automatic detection and segmentation of tumor in breast ultrasound images, *Biomedical Signal Processing and Control* 60, 101945.

Ramos-Llordén, G., Vegas-Sánchez-Ferrero, G., Martin-Fernandez, M., Alberola-López, C., &Aja-Fernández, S.(2015). Anisotropic Diffusion Filter with Memory Based on Speckle Statistics for Ultrasound Images, *IEEE Transactions on Image Processing*, 24(1), 345- 358.

Rodrigues, R., Braz, R., Pereira, M., Moutinho, J.,&Pinheiro, A. M. G. (2015). A two-step segmentation method for breast ultrasound masses based on multi-resolution analysis, *Ultrasound in Biology & Medicine*, 41(6), 1737-1748.

Ridler, T.W., & Calvard, S. (1987). Picture thresholding using an iterative selection method

IEEE Trans. Syst. Man Cybern. Part C Appl. Rev., 8, 630-632

Rodtook, A.,&Makhanov, S. S. (2013). Multi-feature gradient vector flow snakes for adaptive segmentation of the ultrasound images of breast cancer, *J. Vis. Commun. Image R*. 24, 1414–1430.

Rodtook, A., Kirimasthong, K., Lohitvisate, W.,&Makhanov, S. S. (2018). Automatic initialization of active contours and level set method in ultrasound images of breast abnormalities, *Pattern Recognition*, 79, 172–182.

Ronneberger, O., Fischer, P., &Brox, T. (2015). U-net: convolutional networks for biomedical image segmentation. In: *International conference on medical image computing and computer-assisted intervention*, *Springer*, 234–41.

Scott, K., Gelatt, Jr. D.,&Vecchi, M.P. (1983). Optimization by simulated annealing, *Science*, 220 (4598): 671-680.

Selvan, S.,&Devi, S. S. (2015). Automatic seed point selection in ultrasound echography images of breast using texture features, *biocybernetics and biomedical engineering* 35, 157 – 168.

Sha, C., Hou, J., &Cui, H., (2016). A robust 2D Otsu's thresholding method in image segmentation, *J. Vis. Commun. Image R*. 41, 339–351.

Shan, J., Cheng, H. D.,&Wang, Y. (2008). A novel automatic seed point selection algorithm for breast ultrasound images,*2008 19th International Conference on Pattern Recognition*, Tampa, FL, USA, 1-4,

Shan, J., Cheng, H.D.,&Wang, Y.X. (2012). Completely automated segmentation approach for breast ultrasound images using multiple domain features, Ultrasound in Medicine and Biology 38, 262–275.

Shen,J., Hao,X., Liang,Z., Y., Liu,Z., Wang, W.,&Shao, L. (2016). Real-time superpixel segmentation by dbscan clustering algorithm, *IEEE Transactions on Image Processing*, 25 (12), 5933−5942.

Shrimali, V., Anand, R.,&Kumar, V. (2010). Comparing the performance of ultrasonic liver image enhancement techniques: A preference study, *IETE Journal of Research*, 56, 4–10.

Singh, V. K., Abdel-Nasser, M., Akram, F., Rashwan, H. A., Sarker, Md. M. K., Pandey, N., Romani, S.,&Puig, D. (2020). Breast tumor segmentation in ultrasound images using contextual-information-aware deep adversarial learning framework, *Expert Systems With Applications*,162, 113870.

Singh, A.,&Kumar, S. (2020). A novel dice similarity measure for IFSs and its applications in pattern and face recognition, *Expert Systems With Applications*, 149, 113245.

Singh, K., Ranade, S. K.,&Singh, C.,(2017). A hybrid algorithm for speckle noise reduction of ultrasound images, *Computer Methods and Programs in Biomedicine*, 148, 55 – 69.

Sivakumar, V., & Janakiraman, N. (2020). A novel method for segmenting brain tumor using modified watershed algorithm in MRI image with FPGA, *BioSystems* 198, 104226.

Stam, A.T., Thickman, D., C. L. R. et al., (1995). Use of sonography to distinguish between benign and malignant lesions: *Radiology*, 196.

Stavros, A .T. Rapp, C. L.,& Parker, S. H. (2004). Breast ultrasound, 1015.

Sun, C. (1995). Symmetry detection using gradient information.*Pattern Recognition Letters*, 16:987–996.

Sudeep, P.V., Palanisamy, P., Kesavadas, C.,& Rajan, J. (2015). Nonlocal linear minimum mean square error methods for denoising MRI, *Biomedical Signal Processing and Control*, 20, 125–134.

Taha, A.,& Hanbury, A. (2015). Metrics for evaluating 3D medical image segmentation: analysis, selection, and tool, BMC Medical Imaging, 15–29.

Talha,M., Sulong, G.B.,&Jaffar,A. (2016). Preprocessing digital breast mammograms using adaptive weighted frost filter, *Biomedical Research* 27, 1407–1412.

Tana, N., Xu, Y.,Goh, W., &Liu, J. (2015). Robust multi-scale superpixel classification for optic cup localization, *Computerized Medical Imaging and Graphics*, 40, 182–193.

Tang, H., Zhuang, T.,& Wu, E.X. (2000). Realizations of fast 2df3d image filtering and enhancement, *IEEE TMI*, 20, 132-140.

Tania, S., &Rowaida, R. (2016). A comparative study of various image filtering techniques for removing various noisy pixels in aerial image, *International Journal of Signal Process*, 9(3):113–243.

Tian, C., Xu, Y.,&Zuo, W. (2020). Image denoising using deep CNN with batch renormalization, *Neural Networks* 121, 461–473

Vakanski, T., Xian, M.,&Freer, P. E. (2020). Attention-enriched deep learning model for breast tumor segmentation in ultrasound images, *Ultrasound in Medicine& Biology*, 46(10), 2819 – 2833.

Vidya, K.S., Muthu, R.K., Rajendra, A., Vinod, C., Filippo, M., Hamido, F., &Kwan H. (2016). Application of wavelet techniques for cancer diagnosis using ultrasound images: A Review, *Computers in Biology and Medicine*, 69, 97–111.

Vincent, L.,&Soille, P. (1991). Watersheds in digital spaces: An efficient algorithm based on immersion simulations, *IEEE Trans Pattern Anal Machine Intell*, 13 (6), 583-598

Wang, S., Huang, T., Zhao, X., Mei, J., & Huang, J. (2018). Speckle noise removal in ultrasound images by first-and second-order total variation, *Numerical Algorithms*, 78(2), 513-533.

Wang, W., Zhu, L., Qin, J., Chui, Y., Li, B.,&Heng, P. (2014). Multiscale geodesic active contours for ultrasound image segmentation using speckle reducing anisotropic diffusion, *Optics and Lasers in Engineering,*54, 105–116.

Wu, C.Z., Chen, X., Ji, D.,&Zhan, S. (2018). Image denoising via residual network based on perceptual 1oss, *Journal of Image and Graphics*, 23 (10), 1483-1491

Wu, H., Wang, R., Zhao, G., Xiao, H., Liang, J., Wang, D., Tian, X., Cheng, L.,& Zhang, X. (2020). Deep-learning denoising computational ghost imaging, *Optics and Lasers in Engineering* 134, 106183.

Xian, M., Zhang, Y., & Cheng, H.D. (2015). Fully automatic segmentation of breast ultrasound images based on breast characteristics in space and frequency domains, *Pattern Recognition*, 48, 485–497.

Xian, M., Zhang, Y., Cheng, H.D., Xu, F., Zhang, B.,&Ding, J. (2018). Automatic breast ultrasound image segmentation: A survey, *Pattern Recognition*, 79, 340–355.

Xie, W., Li, Y.,&Jia, X. (2018). Deep convolutional networks with residual learning for accurate spectral spatial denoising, *Neurocomputing*,312, 372 -381.

Xu, C.,&Prince, J.L. (1998). Generalized gradient vector flow external forces for active contours, *Signal Processing* 71 (2), 131–139.

Yap, MH, Edirisinghe, EA, &Bez, HE. (2008). A novel algorithm for initial lesion detection in ultrasound breast images, *J Appl Clin Med Phys*. 9(4):181-199.

Yongjian, Y.,&Scott, T.A. (2002). Speckle reducing anisotropic diffusion, *IEEE Trans Image Process*, 11, 1260-1270

Yuan, Y., Chen, Y., Dong, C., Yua, H.,&Zhu, Z. (2018). Hybrid method combining superpixel, random walk and active contour model for fast and accurate liver segmentation, *Computerized Medical Imaging and Graphics* 70, 119–134.

Zhang, J., Wang, Y.,&Shi, X.(2009). An improved graph cut segmentation method for cervical lymph nodes on sonograms and its relationship with node's shape assessment, Computerized Medical Imaging and Graphics, 35(8), 602-607.

Zhang, Y., Xian, M., Cheng, H.D., Ding, J., Xu, F., Huang, K., Zhang, B., Ning, C., & Wang, Y. (2018).A Benchmark for Breast Ultrasound Image Segmentation (BUSIS)," arXiv preprint arXiv:1801.03182.

Zhang, Q., Zhao, X.,&Huang, Q. (2014). A multi-objectively-optimized graph-based segmentation method for breast ultrasound image, *International Conference on Biomedical Engineering and Informatics*, 116-120.

Zhang, M., Zhang, F., Liu, Q., &Wang, S. (2019). VST-Net: Variance-stabilizing transformation inspired network for Poisson denoising, *Journal of Visual Communication: Image Representation*, 62, 12–22.

Zhao, W., Xu, X., Liu, P., Xu, F.,&He, L. (2020). The improved level set evolution for ultrasound image segmentation in the high-intensity focused ultrasound ablation therapy, *Optik - International Journal for Light and Electron Optics*, 202, 163669

Zhou, Z., Wu, W., Wu, S., Tsui, P., Lin, C., Zhang, L.,&Wang, T. (2014). Semi-automatic Breast Ultrasound Image Segmentation Based on Mean Shift and Graph Cuts, *Ultrasonic Imaging*, 36(4), 256 –276.

Zhang M., Zhang L., &Cheng H.D. (2010). Segmentation of ultrasound breast images based on a neutrosophic method*Opt. Eng*., 49 (2010), 117001-117012.

Zhou, S., Wang, J., Zhang, S.et al., (2016). Active contour model based on local and global intensity information for medical image segmentation, *Neurocomputing*, 186, 107–118.

Zhu, H., &Huang, C., (2012). An improved median filtering algorithm for image noise reduction. *Phys Procedia*, 25, 609–616.

BIOGRAPHY

Name — Ademola Enitan Ilesanmi

Education — 2010: Bachelor of Science
(Electronics and Computer Engineering),
Faculty of Engineering and Technology,
Lagos State University, Nigeria.

2017: Masters of Science
(Computer Science),
Faculty of Science,
Ebonyi State University, Nigeria.

Publications

(1) **Ilesanmi, A.E.** *, Idowu, O.P., & Makhanov, S.S. (2020). Multiscale superpixel method for segmentation of breast ultrasound, *Computers in Biology and Medicine*, 125, 103879 (https://www.sciencedirect.com/science/article/pii/S0010482520302328).

(2) **Ilesanmi, A.E.** *, Idowu, O.P., Chaumrattanakul, U., & Makhanov, S.S. (2021). Multiscale hybrid algorithm for pre-processing of ultrasound images, *Biomedical Signal Processing and Control*, 66, 102621 (https://www.sciencedirect.com/science/article/pii/S1746809420305024).

(3) **Ilesanmi, A.E.***, Chaumrattanakul, U. & Makhanov, S.S. Methods for the segmentation and classification of breast ultrasound images: a review. *J Ultrasound*, 1-16. https://doi.org/10.1007/s40477-020-00557-5

(4) Idowu, O.P., Adelopo, O., **Ilesanmi, A.E**, Li, X., Samuel, O.W., Fang, P., Li, G. (2021). Neuro-evolutionary approach for optimal selection of EEG channels in motor imagery based BCI application, *Biomedical Signal Processing and Control*, 66, 102621 (https://www.sciencedirect.com/science/article/pii/S1746809421002184)

(5) Idowu, O.P., **Ilesanmi, A.E**, Li, X., Samuel, O.W., Fang, P., Li, G. (2021). An Integrated Deep Learning Model for Motor Intention Recognition of Multi-Class EEG Signals in Upper Limb Amputees, *Computer Methods and Programs in Biomedicine*, 106121 (https://www.sciencedirect.com/science/article/pii/S0169260721001966)

(6) **Ilesanmi, A.E.***, Ilesanmi T.O. Methods for image denoising using Convolutional Neural Networks: a review. *complex & intelligent systems*, (https://link.springer.com/article/10.1007/s40747-021-00428-4)

(7) **Ilesanmi, A.E.** *, Chaumrattanakul, U., & Makhanov, S.S., A method for segmentation of tumors in breast ultrasound images using Variant Enhanced U-Net, *Biocybernetics and Biomedical Engineering*, 41(2), (2021), 802-818 (https://www.sciencedirect.com/science/article/pii/S0208521621000619?dgcid=author)